Medium Scale Travelling Ionospheric Disturbances sensed with GNSS TEC and SuperDARN

Ian J. Kelley

Thesis submitted to the Faculty of the

Virginia Polytechnic Institute and State University

in partial fulfillment of the requirements for the degree of

Master of Science

in

Electrical Engineering

Joseph B. H. Baker, Co-chair

J. Michael Ruohoniemi, Co-chair

Scott M. Bailey

Wayne A. Scales

July 28th, 2022

Blacksburg, Virginia

Keywords: GNSS, SuperDARN, Ionosphere, MSTIDs

Medium Scale Travelling Ionospheric Disturbances sensed with GNSS TEC and SuperDARN

Ian J. Kelley

(ABSTRACT)

Medium Scale Travelling Ionospheric Disturbances (MSTIDs) are quasi-wavelike structures in ionospheric density that can be sensed using Global Navigational Satellite Service (GNSS) Total Electron Content (TEC) techniques and coherent scatter radars such as the Super Dual Auroral Radar Network (SuperDARN). MSTIDs, especially those observed during quiet times and on the night side, have been known to be driven by electrodynamic instability processes, such as the Perkins instability. In this work, SuperDARN is used in conjunction with GNSS TEC data to investigate MSTIDs during a major geomagnetic storm on September 7-8th, 2017. The interval of this study is in the North American region between 23UT and 3UT, during the peak of the storm, when Kp reached 9. MSTIDs during the interval were investigated by previous studies. However, the roles of electrodynamic instability processes and atmospheric gravity waves (AGWs) in driving the MSTIDs were not determined. GNSS TEC fluctuations associated with the MSTIDs were strong, reaching up to half of background TEC. In SuperDARN, MSTID signatures were observed in power measurements. Meanwhile, SuperDARN line-of-sight (LOS) plasma velocity corresponding to MSTID structures exceeded $\pm$500 m/s. This systemic change in the polarity of SuperDARN LOS velocities is indicative of strong polarization electric fields and therefore driving electrodynamic instability processes. This work therefore presents signatures of storm time electrified MSTIDs in mid-latitude North America.

Medium Scale Travelling Ionospheric Disturbances sensed with GNSS TEC and SuperDARN

Ian J. Kelley

(GENERAL AUDIENCE ABSTRACT)

The upper atmosphere contains a region called the ionosphere, where ionized gas called plasma exists. This plasma can be sensed using satellites and ground-based receivers. Specifically, Global Navigational Satellite Service constellations, such as GPS, are good candidates for this technique. This method yields a column density measurement of electrons and is known as GNSS TEC. Most of the time, GNSS TEC is used in a low resolution format, but a high-resolution format is available. This high-resolution GNSS TEC allows for smaller structures in the ionosphere to be investigated. Ionospheric plasma can also be sensed using ground based radar systems, such as the Super Dual Auroral Radar Network (SuperDARN). Combining GNSS TEC and SuperDARN allows for investigation of disturbed structures in the Ionosphere. These structures include wave-like behavior, with time scales under 30 minutes, called Medium Scale Travelling Ionospheric Disturbances (MSTIDs). When these MSTIDs are investigated during times where the Sun is especially active, some unexpected results are found. Most importantly, SuperDARN radars see plasma velocity behave as if it is affected by MSTID structures. This suggests that the buoyancy force which drives the MSTIDs is an electric force instead of a pressure gradient. This behavior has been shown before, but only at night times, specifically when the Sun is not as active. Therefore, this work presents a new kind of MSTIDs.

Acknowledgments

I would like to thank my advisors, Dr. Mike Ruohoniemi and Dr. Jo Baker for helping me through this process. I am grateful to them for guiding me during my time with the SuperDARN research group. I would like to thank Dr. Bharat Kunduri for his help and patience with me as I persued this work. Thanks also to Dr. Shibaji Chakraborty and Dr. Xueling Shi for their help with programming and understanding SuperDARN and TEC data. Thanks to Mr. Kevin Sterne for his work with the radars and teaching me about their operation. I would like to thank the National Science Foundation for the support they have given the SuperDARN research group. I would also like to thank the friends I made throughout my time at Virginia Tech. Thanks to parents Lara and Nate, and my three sisters Charlotte, Josie, and Hannah, for their love. They have been supportive of me through this whole process.

Contents

List of Figures

List of Tables

List of Abbreviations

ACF (Auto Correlation Function) is an operation performed on a time vs intensity dataset whereby correlation is determined as a function of time lag.

AGW (Atmospheric Gravity Wave) refers to a wave mode in the neutral atmosphere, which has gravity as the driving restoring force.

GLONASS (English: GLObal NAvigational Satellite System, Russian: GlObal'naya Navigatsionnaya Sputnikovaya Sistema) is the Russian Federation's GNSS fleet.

GNSS (Global Navigational Satellite Service) refers to any fleet of satellites intended to provide position, navigation, and timing to users.

GPS (Global Positioning System) is the United States' GNSS fleet.

HF (High Frequency) denotes a band of the electromagnetic spectrum ranging from 30-30 MHz.

IMF (Interplanetary Magnetic Field) The magnetic field in the solar system outside of Earth's influence. Mainly from the Sun. Typically presented as Bx, By, and Bz Cartesian coordinates.

IPP (Ionospheric Pierce Point) is the location where TEC values are mapped to. This is assumed to be at an ionospheric height.

L (L Band) denotes a band of the electromagnetic spectrum ranging from 1-2 GHz.

LOS (Line of Sight) refers to the singe dimensional value of a vector measurement (such as velocity, electric field, etc) in the line between the observed region and the location of the sensor.

LSTID (Large Scale Travelling Ionospheric Disturbance) is a TID with a time period of greater than one hour.

MSTID (Medium Scale Travelling Ionospheric Disturbance) is a category of TIDs with a time period of less than one hour.

PACE (Polar Anglo-American Conjugate Experiment) was the experiment by which the Goose Bay and Halley Station radars were used to show conjugate phenomena.

RTI (Range Time Intensity) is a style of plot where a parameter such as power or velocity is plotted according to time and range axis.

SAPS (Sub-Auroral Polarization Stream) is an active time feature of the mid-latitude ionosphere, whereby a narrow westwards plasma drift occurs co-located with a narrow plasma depletion region based on particle precipitation.

STARE (Scandinavian Twin Auroral Radar Experiment) was a twin bistatic phased array VHF radar in Scandinavia.

SuperDARN (Super Dual Auroral Radar Network) is a global network of HF radars designed to detect plasma convection via LOS measurements of decimeter scale field aligned plasma irregularities.

SymH / AsymH (Symmetric/Asymmetric Horizontal component index) present the 1 minute horizontal ring current intensity, which allows for geomagnetic storms to be characterized.

TEC (Total Electron Content) refers to electron column density measurements, typically between a GNSS satellite and ground based reciever.

TECu (Total Electron Content Units) are units for measuring TEC, where 1 TECu is 10^{16} electrons per square meter.

TID (Travelling Ionospheric Disturbance) is a travelling wavelike perturbations in ionospheric density.

VHF (Very High Frequency) denotes a band of the electromagnetic spectrum ranging from 30-300 MHz.

VTEC (Vertical TEC) is a TEC value which has been corrected for oblique propagation through the ionosphere, in order to remove effects from satellite elevation angle.

Chapter 1

Introduction

1.1 Ionosphere

The ionosphere is defined as the region of Earth's upper atmosphere which contains ionization, endowing it with electrical properties. The ionosphere can start as low as 50km in altitude and extend beyond 1000km. The ionosphere is classified into three layers, known as the D, E, and F regions. Usually, most of the ionization is found in the F region. This is typically located between 150 and 1000km altitude. The F region has the highest plasma density and the lowest neutral density of the three. During the day, two peaks sometimes form in the F region, and are denoted as F1 and F2. The F2 layer is the higher of the two (above 200km) and almost always of higher density. In this region, loss through recombination is slow, so it is mostly sustained at night. The F region exists above the less dense D and E regions. These layers are shown in Figure 1.1. The D region is below 100km, and is the weakest. Neutral density is high in this region, and collisions are important. In this region, sustained photo-ionization is needed, so it does not exist at night. The E region exists between roughly 90 and 150km, and is usually less dense than the F region. The E region is sometimes a source of denser plasma, known as sporadic E.

In the ionosphere, most ionization occurs from photo-ionization by the Sun during the day. However, plasma can travel along field lines from the magnetosphere to the auroral ionosphere. This process is known as particle precipitation, and injects energy into the iono-

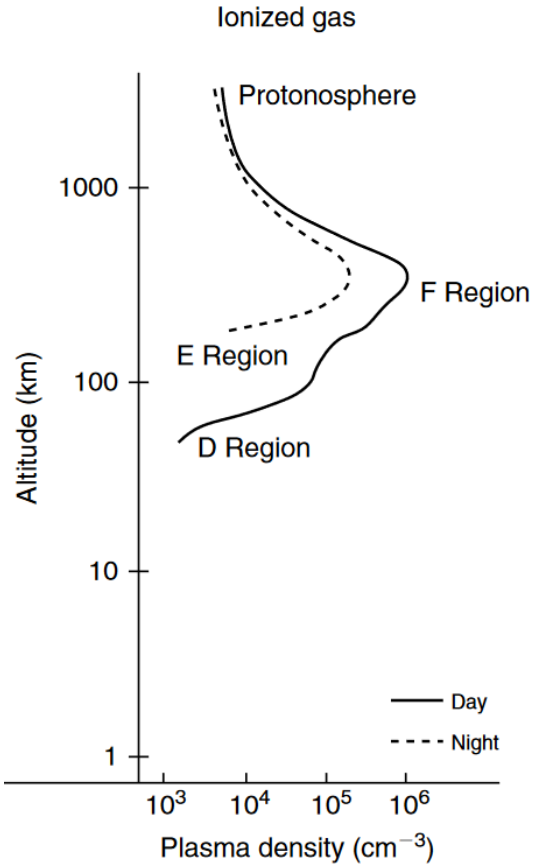

Figure 1.1: Logarithmic altitude profile of plasma density in the ionosphere. The daytime and nighttime ionosphere is shown, with the different layers labelled as D, E, and F. This figure is taken from (Kelley, 2009).

spheric system.

1.1.1 Geomagnetic Storms and Indicies

At higher latitudes, the magnetic field lines of the earth interact with those from the Sun, known as the IMF. The Sun streams out plasma, known as solar wind, at all times. However, this process is variable based on factors such as the 11 year solar cycle, direction, and processes within the Sun's surface. The meeting place between Earth's magnetic field and the IMF is known as the bow shock, which is well outside the Earth's atmosphere (typically

$14R_e$). During periods of intense solar wind, the bow shock is compressed and the tail of Earth's magnetic field is elongated. During these periods, the IMF connects with the Earth's magnetic field on the day-side. This allows solar wind plasma to enter Earth's magnetosphere. Some of this plasma travels back along Earth's field lines to the ionosphere. This can also occur on the night side in the magnetotail, in a process known as a substorm. These likely occur when Earth's field lines re-connect to themselves. These processes are the basis for auroral precipitation. This acts to close a magnetospheric circuit in the ionosphere. Resistance in this region causes heating, known as Joule heating. Energy from this process may be a pertubation source for wave-like disturbances in the ionosphere, called Travelling Ionospheric Disturbances (TIDs). In fact, Joule heating is likely the source of the TIDs discussed in this work.

The planetary K index is a general indicator of geomagnetic activity. It is based on a global algorithm which combines horizontal magnetic field measurements of maximum horizontal deviation. The Kp index categorizes the September 7-8th 2017 event as a 9 out of a possible 9. Thus, this is a highly disturbed period. Other geomagnetic indicies used in this work include solar wind and IMF data taken from NASA OMNI values, with a 1 minute time resolution (King and Papitashvili, 2005). These values have been time-shifted to coincide with the location where the bow shock intersects with the Earth-Sun line. Asymmetric (Asym-H) and symmetric (Sym-H) disturbance indices (Iyemori, 1990) are used to characterize the ring current during the event. Also, the auroral electrojet is characterized via the AL and AU indices (Davis and Sugiura, 1966).

1.2 Travelling Ionospheric Disturbances

Traveling Ionospheric Disturbances (TIDs) are wave-like structures which propagate through the ionosphere. TIDs are most commonly expected to be driven by Atmospheric Gravity Waves (AGWs) originating in the neutral atmosphere. TIDs are further classified as either Large-Scale (LSTIDs) or Medium-Scale (MSTIDs) based on their spatio-temporal scales (Georges, 1968). MSTIDs typically have a time-period of 15-60 minutes, phase velocities of 100-300 m/s, and wavelengths between 200-800km. On the other hand LSTIDs have phase speeds between 400-1000 m/s, periods above 30 minutes, and wavelengths above 1000 km (Hocke and Schlegel, 1996; Hunsucker, 1982). In this section, ionospheric disturbances, such as gravity wave driven TIDs, will be discussed. Also, the concept of electrified TIDs will be presented. Finally, previous studies of TIDs using SuperDARN and GNSS TEC will be discussed. Emphasis will be placed on the differences between AGW-driven and electrified TIDs, and MSTIDs in particular.

1.2.1 Atmospheric Gravity Waves

Atmospheric gravity waves are the basis for the majority of TID studies. AGWs are a neutral atmospheric phenomena whereby gravity acts as a restoring force following a perturbation (Hines, 1960). Munro (1948) observed wave activity in the ionosphere which was eventually linked to the behavior of AGWs (Georges, 1968; Hunsucker, 1982; Hocke and Schlegel, 1996). AGWs drive ionospheric density perturbations primarily because enhanced neutral density causes enhanced ion-neutral collisions. This in turn changes the ion altitude distribution. Recombination rates change and therefore a wave in the neutral atmosphere is manifested in the ionospheric plasma. Neutral gravity waves in the atmosphere are seeded by a number of perturbations, both from Earth and space. Polar vortexes (Frissell et al., 2016), explosions

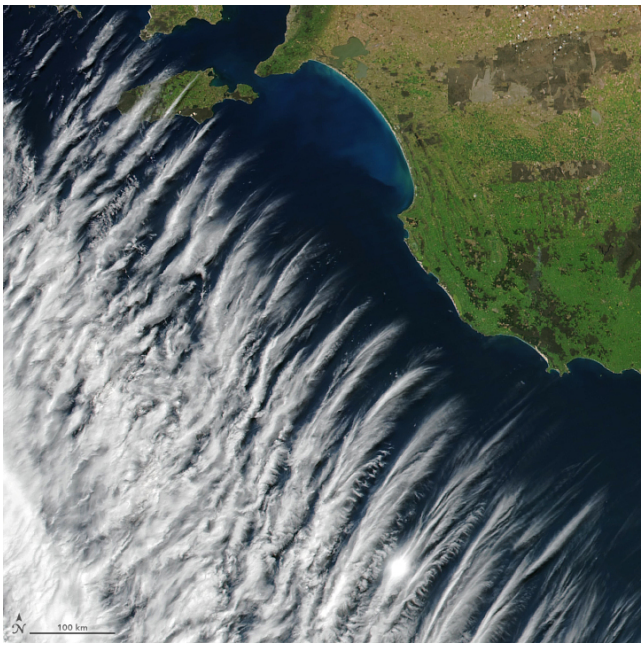

Figure 1.2: NASA Earth Observatory image taken from Suomi NPP satellite showing gravity wave signatures in tropospheric clouds over Southern Australia. Image is from (Hansen and Stevens, 2017)

such as the Beirut explosion (Jonah et al., 2021), and earthquakes (Liu et al., 2011) can all cause AGW driven TIDs. MSTIDs under this regime may also be caused by auroral sources via space weather as described by (Chimonas and Hines, 1970) and observed in (Samson et al., 1990; Bristow et al., 1994, 1996). In general, AGW-driven MSTIDs peak during daytime, in the winter months, and propagate equator-wards (Samson et al., 1990; Frissell et al., 2014; Grocott et al., 2013; Kotake et al., 2006). An example of an AGW is shown in Figure 1.2. Like typical gravity waves, this feature contains regular density fluctuations which are aligned perpendicular to the propagation direction. Not all AGWs are visible as features within clouds. Also, not all AGWs reach ionospheric heights and manifest as TIDs.

1.2.2 Electrified TIDs

Studies of TIDs eventually yielded some unexpected observations. Using the Arecibo observatory, it was found that some structures contained strong internal electric fields, and high plasma drifts as a result (Behnke, 1979). This was unexpected but repeatable in later studies using ground based radar systems (e.g., Fukao et al., 1991; Kelley and Fukao, 1991), 630nm airglow observations (e.g., Garcia et al., 2000; Mendillo et al., 1997), and even in conjugate observations by the DE2 satellite (Saito et al., 1995). A mid-latitude plasma instability known as the Perkins instability (Perkins, 1973) was suggested as the reason for this phenomenon. The equation for the growth rate of the Perkins instability (γ) is

$$\gamma = \frac{c \cos D}{B H_n} E_0 \sin(\theta - \alpha) \sin \alpha$$

where c is the speed of light, B is the geomagnetic field intensity, D denotes the magnetic dip angle, and H_n is the scale height of the atmosphere. E_0 is the electric field, either from the neutral wind ($E_0 = U \times B$) or background ionospheric field. θ is the horizontal angle of the background electric field and α is the angle of the perturbation vector (both with respect to magnetic east). The Perkins instability exists in regions where field lines have both a vertical and horizontal component, such as the mid-latitude ionosphere. In this region, a horizontal electric field interacts with a horizontal magnetic field component. Provided the correct orientation, a vertical force in the $E \times B$ direction is imparted to the plasma. This force acts similarly to the buoyancy force in the AGW regime. Kelley (2011) coined the term "electrobuoyancy" to describe this situation. However, this force exists only for specific orientations of the background electromagnetic fields, as demonstrated in the growth rate equation. Westwards propagation is preferentially supported in the mid-latitude northern hemisphere. The physical basis for this is the $E \times B$ drift velocity and the gravity-collision

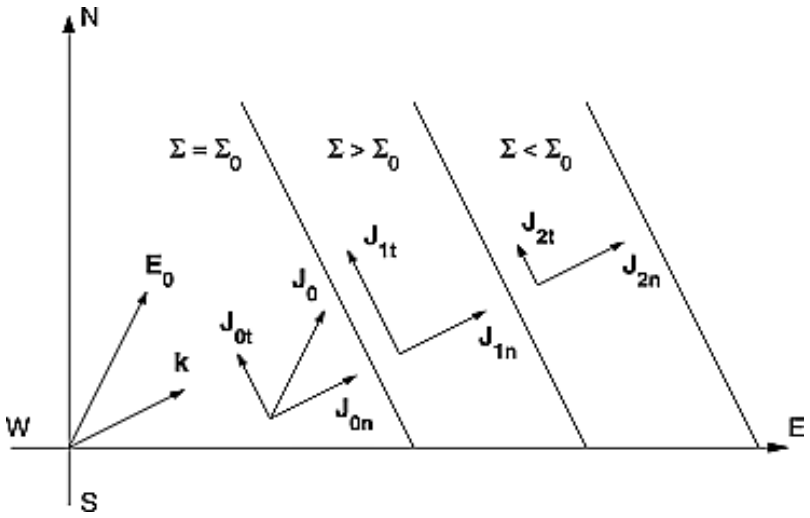

Figure 1.3: Currents which arise as a result of an electrified TID. The background ionospheric case is shown as $\Sigma = \Sigma_0$. The TID contains bands of increased ($\Sigma > \Sigma_0$) and decreased ($\Sigma < \Sigma_0$) conductivity based on plasma density. Note that $J_{0n} = J_{1n} = J_{2n}$ and $J_{1t} > J_{0t} > J_{2t}$. This illustration is taken from Figure 1b from (Zhou and Mathews, 2006).

velocity causes perturbed layers to drift away from equilibrium in these orientations (Zhou and Mathews, 2006). Meanwhile, in other orientations, these drifts act towards equilibrium, damping the instability.

Polarization electric fields arise based on current continuity. This is illustrated in Figure 1.3, where a TID is shown in relation to the background ionosphere. In this scenario, a divergence free condition is assumed. This means that current normal to the TID wave fronts must be constant. However, conductivity is not constant, and varies with the plasma density fluctuations of the TID. The consequence is that polarization electric fields arise within the structures of the TID. In the case of Figure 1.3, a background electric field E_0 is present with a component in the TID direction (k). This means that a polarization field is created opposite the k direction in the $\Sigma > \Sigma_0$ region and in the k direction in the $\Sigma < \Sigma_0$ region.

During most electrified MSTID events, quiet conditions are present, limiting the electric field

to 1 mV/m in the equatorward direction (Kelley, 2009). The neutral wind is the dominant source of electric field, and its force acts in the $U \times B$ direction. This neutral wind electric field is the basis for most studies which address electrified MSTIDs. Additionally, the presence of sporadic E has been found to be necessary for electrified MSTIDs to occur (Narayanan et al., 2018) in quiet time conditions. This is because it has been shown that one night is not long enough for the instability to grow sufficiently in the F region alone (Garcia et al., 2000).

Global Navigational Satellite Service Total Electron Content (GNSS TEC) has been used extensively to study electrified TIDs (e.g., Saito et al., 1998; Otsuka et al., 2004, 2007, 2009). GNSS TEC is an integrated column plasma density measurement technique. Based on assumed ionospheric plasma density profiles (Figure 1.1), TEC is used as a proxy for peak electron density. GNSS TEC is described in detail in the following section.

While ground-based radar studies began with VHF radars, HF radars such as SuperDARN have been used to study these phenomena (e.g., Ogawa et al., 2009; Hazeyama et al., 2022). Through all these studies, a set of differences between AGW and electrified TIDs has been established, which is summarized in Table 1.1. Note that differences in time and season are important. For this reason, MSTIDs are sometimes categorized as night or day as a proxy for AGW vs electrified. So far, electrified MSTIDs have been accepted as a night-side, quiet time phenomena. However, MSTIDs which exhibit some electrified properties have been observed outside of these conditions, such as the storm time event which is the basis for this work.

Direction alone can be used to suggest that MSTIDs may be electrified, but more measurements are needed to be certain. Specifically, a dataset which can demonstrate the presence of polarization electric fields is needed. Alternatively, observations of plasma motion which follows the $E \times B$ convention can demonstrate the required electric field behavior. Super-

Table 1.1: Features of AGW and Electrified TIDs

Feature	AGW TIDs	Electrified TIDs
SuperDARN Power	focusing ground scatter	ionospheric irregularities
SuperDARN LOS Velocity	almost none	high LOS oscillations
GNSS TEC Observation	electron density waves	electron density waves (same)
Driver	neutral atmospheric waves	plasma instability, seeded by AGWs
Time	winter, day	summer, night
Location	high latitude	mid-latitude
Polarization E-fields	none	parallel to propagation
Conjugacy	no	yes
Direction	equatorwards	westwards preferred

DARN radar data is used in this work alongside GNSS TEC to show electrification of the MSTIDs presented in (Zhang et al., 2019).

1.3 GNSS TEC

TEC used in this study is based on measurements of GNSS satellite signals by ground-based receivers. In this section, the history and present state of GNSS constellations are discussed. Equations for deriving GNSS TEC are shown, and TEC measurement techniques are explored. The high-resolution global TEC dataset used in this work is explained, as well as the way in which it is de-trended to show phenomena such as MSTIDs.

1.3.1 Global Navigational Satellite Service

Satellite navigation is a concept whereby satellites at a known position transmit a time stamp via a radio wave. Through line of sight propagation, receivers estimate the distance to each satellite and can derive position. Other information such as speed and time can be found as well. Satellite navigation dates back to the first man-made satellite, Sputnik 1, launched

in 1957. In measuring the Doppler frequencies, it was determined that it was possible to pinpoint the Sputnik's location within its orbit (Guier and Weiffenbach, 1960). By reversing this problem, it was possible to determine receiver location if the orbital characteristics of the satellite were known. Based on this principle, the United States launched the Transit satellite fleet starting in 1959. The system was in operation by 1960 and allowed for military and later civilian users to determine their location. However, not enough satellites were available for continuous coverage, and users had to deal with long wait times and poor accuracy.

Starting in 1967, the Timtation satellite fleet was launched, which featured accurately disciplined clock oscillators. These clocks eventually included atomic clocks, allowing ground users to access accurate time data from anywhere on earth. Combining these highly disciplined clocks with the Transit system allowed for a new form of satellite navigation. By knowing the position of the satellites and measuring the distance (as opposed to Doppler velocity) of the satellite, a navigational solution was determined. In this format, timing is highly important, since the distance is measured as line of sight propagation at the speed of light. Four satellites are needed for a valid navigational solution, with three for position and one for correcting receiver clock offset. This allows for low cost receiver side hardware, which eventually allowed for widespread civilian use of Global Navigational Satellite Service (GNSS) technology.

American Global Positioning Service (GPS) was the first GNSS constellation, with launches starting in 1978. By 1993, the full fleet was operational (Getting, 1993). GPS satellites orbit at an altitude of 20,200 km in a 12 hour orbit, called semi-synchronous, as two orbits are completed each sidereal day. Therefore, GPS satellite passes repeat themselves from the perspective of a ground user every 12 hours. Their altitude also means that satellite passes are often several hours long. Meanwhile, low earth orbit satellite passes may be just a few minutes.

Many critical systems place reliance on GPS, including the Military. For this reason, redundancy is important. The GPS constellation has 31 operational satellites. Of this number, 24 satellites are active, with the rest acting as spares. At any one time, approximately six satellites are visible to a ground user, which is more than sufficient for a navigational solution, provided none are obstructed.

GPS satellites broadcast right-hand circularly polarized radio waves. Signals are spread into a CMDA waveform, and the de-spreading gain provided by this format helps offset the low receiver power. This receiver power level has a minimum value of -128 dBm ($1.5 \times 10^{-16} Watts$), which is far below the noise floor before de-spreading. This received power is far lower than other forms of radio communication. Its cause is low transmitter power (30 Watts), high path loss (20,200 km), and omni-directional receiver antennas. Each satellite broadcasts a different known pseudo-random noise code, which allows for satellite identification. Additionally, this system ensures signal orthogonality between multiple satellites on the same bandwidth. The two most used frequencies are L1 (1575 MHz) and L2 (1227 MHz). In each signal, different codes are present for different users. The Coarse Acquisition (C/A) code is the simplest of these, and designed for low-cost civilian use. C/A signals are modulated as 50 bit/s BPSK on top of CDMA spread to a ratio of 1023. Therefore, spreading gain is on the order of +30dB. GPS also contains Precision Secure (P/Y) codes, which were originally intended for military users. GPS modernization starting in 2005 introduced a new L2C code for civilian use of the L2 signal, as well as a Military (M) encoded signal to bolster the security of the constellation against jamming and decryption. This was intended to replace the P/Y signal. A new L5 signal (1176 MHz) was added as well for increased accuracy and compatibility with other constellations. This lower frequency signal performs better in environments where line-of-sight propagation is challenging. Typical mass market receivers make use of just the L1C code, which was originally designed for acquisition. This contains

Table 1.2: GPS and GLONASS Charactaristics

Charactaristic	GPS	GLONASS
Country	USA	Russia
Altitude	20,200 km	19,100 km
Inclination	55°	68°
Period (hh:mm)	11:58	11:16
Number of Operational Satellites	31 (24 active, 7 spare)	24
Navigation Format	Keplerian Orbital Parameters	Cartesian Coordinates
Navigation Updates	30 minutes	2 hours
Unique Orbital Planes	6	3
Data rate	50 bits/s	50 bits/s
Code Access	FDMA / CDMA	Only CDMA

errors from ionospheric effects, which ideally would be corrected for (Klobuchar, 1987). More advanced hardware sometimes makes use of both the L1C and L2C signals. This allows for removal of ionospheric delays, which is the largest source of navigation error. A side-effect of this premise is an ability to measure ionospheric electron column density. This principle is the basis for measuring Total Electron Content (TEC). The GPS data used in this work is therefore based off TEC data obtained from the L1C and L2C signals.

The first GLONASS satellite launched in 1982, with the constellation coming to completion in 1995 under the new Russian Federation. However, the Russian economic crisis led to budget cuts. In this period, not enough satellites were in orbit for users to have enough visible at all times, which continued until 2010. GLONASS satellites operate similarly to their GPS counterparts, with a few key differences (See Table 1.2). GLONASS satellites orbit at 19,200 km at a 68° inclination. This is higher than the GPS inclination (55°) allowing for better polar coverage. GLONASS satellites also transmit their location in Cartesian coordinates every 30 minutes, which removes the need to translate orbital parameters. Meanwhile, GPS only broadcasts satellite Keplerian orbital parameters every 2 hours. GLONASS signals also incorporate FDMA, meaning different channels are used for different satellites. This further reduces interference, and potentially makes code identification simpler. For many

applications, both GPS and GLONASS are used to provide extra accuracy and reliability by complementing each other. For example, vehicles travelling in urban areas which do not have enough visible satellites and may benefit from using both constellations (Angrisano et al., 2012).

GLONASS and GPS are used in the following work. However, other GNSS constellations exist. Galileo is the European Union's constellation and BeiDou is China's. Other nations operate regional systems, such as India's NavIC and Japan's QZSS. Some of these systems contain satellites at higher altitudes in order to remain in view of a specific region of the earth at all times. The process of augmentation, whereby additional information is used to improve the quality of GNSS, is also widespread. In recent years, efforts have been made to increase compatibility between GNSS constellations, such as a universal L5 signal at a lower frequency.

1.3.2 Total Electron Content

TEC is a well established measurement which reports the column electron density between a transmitter and receiver using dual frequency radio delays. Because most electrons in the atmosphere exist in a relatively thin layer, this measurement is often used as a proxy for peak ionospheric electron density. TEC measurements do not need to be sourced from GNSS satellites, and geostationary dual frequency transmissions have been used as a source of TEC data (e.g. Kunitsyn et al., 2016). However, most TEC datasets make use of GNSS satellites due to their high altitude, standardized transmission, and widespread distribution. The first TEC measurements go back to Sputnik satellites (Lawrence et al., 1963) and the first GNSS TEC measurements were accomplished using Faraday rotation of the GPS L1 C/A code. This is partially because the L2C code was not available until GPS modernization.

However, modern GNSS TEC measurements are usually based on a dual frequency range error estimation of refractive index, explained in detail below.

The speed of the electromagnetic wave is defined in two ways: both the speed of a phase front (phase speed) and the speed of envelopes within the waves (group speed). In a vacuum, these values are the same. However, this is not true under dispersive conditions, such as inside ionospheric plasma. Phase and group speed for electromagnetic waves can be written as

$$v_p = \frac{\omega}{k} \qquad v_g = \frac{\partial \omega}{\partial k}$$

respectively, where ω is the angular wave frequency and k is the wave number. The equation for wave frequency for electromagnetic waves in a cold, un-magnetized plasma (such as the ionosphere) can be written as

$$\omega^2 = \omega_{pe}^2 + k^2 c^2$$

where c is the speed of light in a vacuum ($3 \times 10^8 m/s$) and ω_{pe} is the electron plasma frequency. In this case, the ions are assumed to be stationary due to their higher inertia. Under conditions where the wave frequency is less than the plasma frequency, propagation through the plasma is not supported. The wave can even bounce off the plasma, provided its frequency is significantly lower than the plasma frequency. This is due to an impedance mismatch between media. In cases where the frequencies are similar, energy from incident waves are absorbed by electrons oscillating at the plasma frequency. The equation for electron plasma frequency in a cold plasma can be written as

$$\omega_{pe} = \sqrt{q\frac{n_e}{\epsilon m_e}}$$

where n_e is the electron density, q is the elemental charge ($1.6 \times 10^{19} C$), ϵ is the permittivity of free space ($8.85 \times 10^{-12} F/m$), and m_e is the mass of an electron ($9.1 \times 10^{-31} kg$). All of these values are constant besides the electron density. Based on these equations, the group velocity can be written as

$$v_g = \frac{\partial \omega}{\partial k} = \frac{kc^2}{\omega} = c\sqrt{1 - \frac{\omega_{pe}^2}{\omega^2}}$$

Note that the phase speed equation has been plugged in for the k/ω term. This group velocity can be further simplified, depending on the ratio of the wave frequency to the plasma frequency. In cases such as GNSS signals in the ionosphere, a characteristic wave frequency is 1.5 GHz, while the ionospheric peak electron plasma frequency (foF2) is typically 2-20 MHz. Because the wave frequency is much higher than the plasma frequency, group velocity can be simplified to

$$v_g = c\left(1 + \frac{\omega_{pe}^2}{2\omega^2}\right)$$

However, the ground-based GNSS receivers measure time delay, not group velocity. The group velocity equation can be re-arranged into a time equation through the entire length of the propagation path as

$$t = \int \frac{1}{c} dr + \int \frac{\omega_{pe}^2}{2c\omega^2} dr$$

The second term of this equation is the additional time delay caused by the plasma, which

would not be present in a vacuum. The time delay relative to vacuum propagation is therefore of interest as it is only affected by electron density. This time delay can be written and simplified as

$$\delta t = \int \frac{\omega_{pe}^2}{2c\omega^2} dr = \int \frac{n_e q^2}{2c\epsilon m_e \omega^2} dr = \frac{40.3}{cf^2} \int n_e dr$$

where $\int n_e dr$ is the column electron density, and hence the TEC. However, only t and not δt is known for any one GNSS signal. At least two signals, such as GPS L1 and L2, allow for measurement of $\delta t_1 - \delta t_2$. TEC is derived using this dual-frequency difference measurement. The equation for it is written as

$$TEC = (\delta t_1 - \delta t_2) \frac{c}{40.3} \frac{f_1^1 f_2^2}{f_2 - f_1}$$

where f_1 is a lower frequency than f_2. For both GPS and GLONASS satellites, f_1 is typically the L2C signal while f_2 is typically the L1C signal.

1.3.3 Hi-Resolution Global TEC

A global network of ground based satellite receivers is used to provide TEC data to the public. This data comes in two formats. The binned format has a resolution of one degree latitude by one degree longitude and a temporal resolution of five minutes. This is sufficient for many studies, but not for MSTIDs which may have smaller scales. The higher resolution format, which is used in this work, is available with 30 second temporal resolution. Instead of binning measurements, each individual IPP measurement is provided in the file. This data format is useful in sensing smaller scale structures such as TIDs (Saito et al., 1998), and in particular MSTIDs (Tsugawa et al., 2007). The data is summarized in Table 1.3.

In this format, the TEC value provided is as accurate as possible in both the absolute sense and the relative sense. This means the actual value, as well as its relative changes are accounted for as much as possible. This is accomplished using both the pseudorange and phase range measurements. Furthermore, receivers may experience bias due to ambient temperature, F10.7cm flux, and other factors (Coster et al., 2013). However, the main factor which causes uncertainty in using TEC as a proxy for ionospheric peak electron density is elevation angle. Based on the angle the radio wave takes through the ionosphere, higher electron content values are measured. The lowest possible TEC measurement through a given pierce point in the ionosphere is obtained when the satellite-receiver link is in the zenith direction. In practice, TEC measurements are usually translated to a "vertical" measurement by correcting for a known elevation angle. This is known as VTEC. This is standard practice in most data aggregated from many receivers, such as the global data used in this work. High-resolution global TEC has slant TEC corrected using the following mapping function defined in (Rideout and Coster, 2006)

$$VTEC = TEC\sqrt{1 - (Fcos(e))^2}$$

where e is the elevation angle and F=0.95 is an adjustment parameter which reduces error between measurements. This function's goal is not only to correct for elevation, but to ensure that measurements of the same ionospheric sample from different receivers yield the same result. These corrections are done before data is released, so users do not need to perform them. The result is a high quality global dataset which is accurate and ready to be used for scientific studies. Both the GPS and GLONASS GNSS constellations are used for this data. This data is available at `www.http://cedar.openmadrigal.org` and is provided by MIT/Haystack Observatory. An example of this data, binned to a 1 by 1 degree size in five minute time resolution, is shown in Figure 1.4. In this view of North America, TEC shows

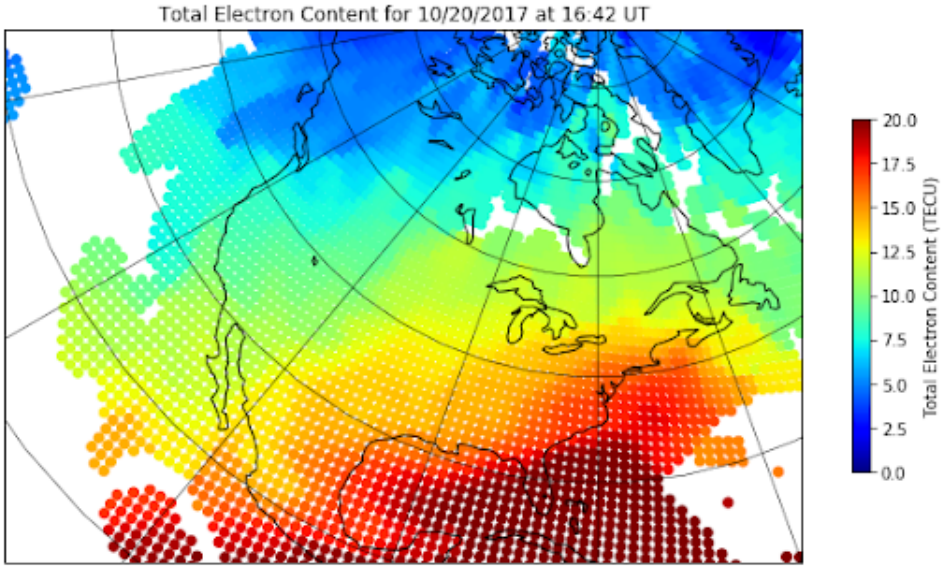

Figure 1.4: GNSS TEC over North America on October 20th, 2017. TEC is binned into a 1 by 1 degree format available in a 5 minute time resolution from www.http://cedar.openmadrigal.org. This figure was generated with data from this source.

the basic density structure of the ionophere, even in a low resolution format. Large-scale features such as LSTIDs can be perceived in this format. However, each data point is 1 degree wide in longitude, meaning that data is of a significantly higher zonal resolution in the higher latitudes. This makes studying meso-scale structures particularly challenging at lower latitudes. In many cases, a higher resolution data is preferable. Because of this, a line of sight format which retains each individual IPP in a 30 second time resolution is also distributed.

High-resolution TEC is time-stamped at 0 and 30 seconds of every minute for the entire day. For each time-stamp, many thousands of data points are present. One issue in this data is drop-outs. Often, an individual time will only see a fraction of the data typically present. This is challenging when making animations and maps. A solution for this is to check the number of data points at each time and remove the entire period if there is a drop-out. In other cases, such as static plots, these drop outs are left in, and often visible in plots. This

Table 1.3: Hi-Resolution TEC Data Charactaristics

Data Label	Description
timestamp	time data was taken
latitude	geographic latitude of IPP
longitude	geographic longitude of IPP
TEC	absolute VTEC measurement in TECu
GPS site	unique code for each ground based receiver
Satellite ID	unique code for each GNSS satellite
elevation	angle of elevation between satellite and receiver

issue is persistent in the data, and is present at the source.

1.3.4 De-Trending GNSS TEC

TEC is often dominated by local time effects, and other large scale features. Some applications, such as scintillation (Mitchell et al., 2005), eclipses (Coster et al., 2017), or TIDs (Zhang et al., 2019), may not rely on absolute values, but rather relative changes in TEC. In these cases, TEC can be used to identify smaller trends not visible in the original data. Such a "relative" TEC measurement is often accurate to 0.01 TECu (Coster et al., 2013), which is higher than TEC in the absolute sense, due to the nature of the measurement. MSTIDs are a good candidate for de-trended high-resolution TEC due to their shorter period, lower amplitude, and smaller spatial scale than LSTIDs.

In order to de-trend TEC data, the original source satellite and receiver of each data point must be known. Both of these are available in TEC data (Table 1.3). Data files cover the entire globe for a whole day. Because of this, the size of these files is often many Gigabytes, typically containing hundreds of millions of individual TEC measurements. In order to perform operations, such as de-trending, the size of the data needs to be greatly reduced. In many cases, such as in this work, only a small geographic region or time period is of interest. Data which is outside this region of interest should be removed first to make de-trending

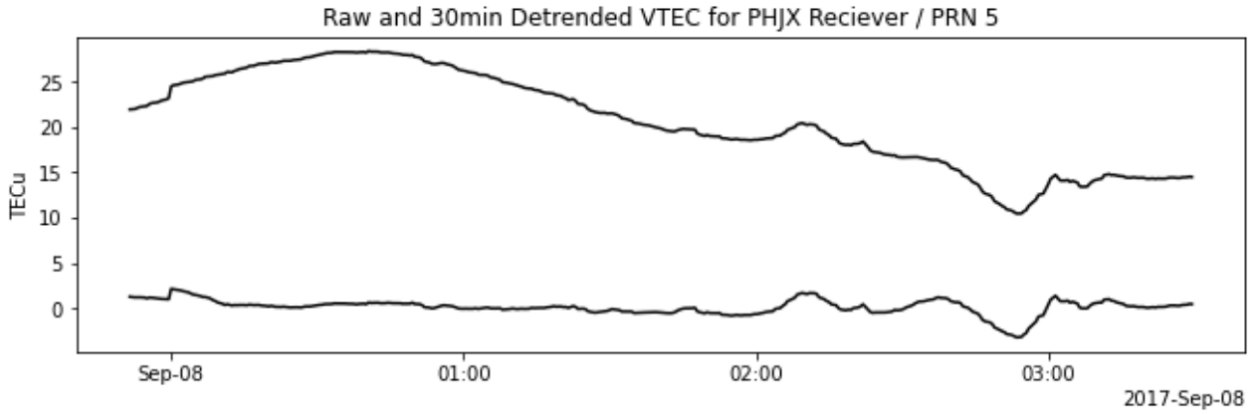

Figure 1.5: Raw (top) versus de-trended (bottom) TEC for a single satellite-receiver pair. De-trending operations involved subtracting a 30 minute rolling average from the raw data. Around 30,000 of these individual time series needed to be de-trended for 3 hours of data over the US.

easier. Data values obtained below a certain elevation angle ($< 30°$ is used in this work) are also removed. This standard practice is done to reduce uncertainty from long oblique paths through a thin ionospheric layer. If left in, these measurements may display inaccurate TEC values which are unintentionally influenced by changing TEC, scintillation, and other uncertainties. Also, the recorded TEC data values contain unnecessary significant figures, which take up excess space in data files.

Once unnecessary data has been removed, a 30 minute rolling average is subtracted from each satellite-reciever pair, as shown in Figure 1.5. Thus, trends of less than 30 minutes in period are preserved, while longer trends are removed. In practice, this involves running a rolling average over all of the data, which is a time consuming process. Individually de-trending 30,000 of these time-series would not be viable. Instead, the data is re-ordered and then de-trended as one long time series. Data comes ordered by time stamp and then by satellite-receiver pair. Re-ordering data by satellite-receiver and then by time stamp allows the whole data-set to be ordered as a time series. The time savings on processing using this method are significant. Originally, de-trending for just three hours of US based receivers took

many days to run. By re-ordering the data, de-trending the same data takes just 15 minutes to an hour on an average computer. The Pandas (Wes McKinney, 2010) Python package was used for data operations, including calculating and subtracting the rolling average.

De-trending TEC has been reported in previous studies (e.g., Coster et al., 2013; Lyons et al., 2019; Zhang et al., 2019), including using a 30 minute window. Often, the de-trending method used in these studies is more intensive than the one reported here. For example, re-sampling of the data allows for drop-outs to be removed. Additionally, high frequency noise is removed in some cases via edge effects. In contrast, the approach taken in this work is to simply subtract the rolling average from each satellite-receiver pair. This allows for significantly faster data processing. Depending on the ionospheric phenomena, de-trending may be more or less consequential. For example, strong MSTID signatures may not rely on de-trending to the same degree as weaker signatures.

1.4 SuperDARN

SuperDARN is a global network of HF radars, which are primarily designed to capture plasma convection in the ionosphere. In the following section, the history of SuperDARN will be discussed. Furthermore, SuperDARN data will be explained and defined. Finally, the use of SuperDARN for studies of TIDs will be reviewed.

1.4.1 History of SuperDARN

SuperDARN was preceded by various coherent scatter radars, which primarily operated in the VHF band. The Scandinavian Twin Auroral Radar Experiment (STARE) operated a set of bi-static radars (Greenwald et al., 1978). This experiment allowed for 2D mapping of

plasma convection. However, one major issue with VHF at high latitudes is that irregularities in the F region are not visible to the radar because with straight line propagation the rays do not propagate orthoginally to field lines at these altitudes. Similar systems were built around the same time period. These include the Sweden And Britain Radar Experiment (SABRE) (Nielsen et al., 1983) and the Bi-static Auroral Radar System (BARS) (McNamara et al., 1982). For a more comprehensive history of coherent scatter ionospheric radars before SuperDARN, see (Greenwald, 2021).

The first SuperDARN radar was built in Goose Bay, Labrador, Canada in 1983. First results from this radar are presented in Greenwald et al. (1985). This system is still operational today. A similar HF radar was built for the Halley Station, Antarctica. This became the first Southern Hemisphere SuperDARN radar. The purpose of this station was to observe geomagnetically conjugate behavior between hemispheres. Specifically, these two radars observed a geomagnetically conjugate region. These two radars were the basis for the Polar Anglo-American Conjugate Experiment (PACE) (Baker et al., 1989). A second Northern Hemisphere radar was also built in Scheverville, Quebec, Canada. While it is possible to map plasma motion using a single radar (Ruohoniemi et al., 1989), using two radars with overlapping fields of view allows for a more accurate picture of plasma convection (Freeman et al., 1991). Using radars with overlapping fields of view allowed for a Dual Auroral Radar Network (DARN) (Greenwald et al., 1995). However, the location of the Schefferville radar was not optimal for measuring higher altitude F region plasma convection. This is because Goose Bay is only 500 km from Schefferville. A subsequent radar built in Stokkseyri, Iceland, allowing the first dual measurements of F region plasma convection. Following the original SuperDARN blueprint, many radars were constructed across Earth's polar and high latitude regions. Some radars were constructed in inhospitable regions, including several in the Antarctic continent. Across the next decade numerous scientific achievements stemmed

from the widespread construction of additional radars (Chisham et al., 2007).

In the 21st century, SuperDARN expanded its coverage to include mid-latitude regions. This is primarily because the auroral oval expands during geomagnetic storms. Therefore, lower latitude SuperDARN radars are more suited for capturing disturbed time phenomena. Baker et al. (2007) demonstrates this using the Wallops radar, which was the first mid-latitude SuperDARN radar. Expanding to these middle latitudes also featured easier areas of the globe to access, and allowed for many additional radars to be built. Newer radars feature updated electronics and better performing twin terminated folded dipole antennas. Nishitani et al. (2019) reviews the achievements of mid-latitude SuperDARN, across various scientific topics. Across the world, over 30 radars are in operation today, including polar, high, and middle latitude radars. A map of current SuperDARN coverage is shown in Figure 1.6. In the future, even lower latitudes may be of interest. Equatorial radars have been shown to be viable, especially in the African region (Michael et al., 2020). These equatorial radars will have to deal with horizontal field line geometry. Various phenomena such as the equatorial electrojet and plasma bubbles are unique to this region.

1.4.2 SuperDARN Data

SuperDARN radars use coherent scatter radar techniques. This means that instead of sensing backscatter from individual electrons, radars are sensitive to irregularities in electron density. Specifically, density irregularities need to be on a scale comparable to the half the wavelength of the signal. This also meant that early VHF radars were limited in their ability to sense larger irregularities. In coherent scatter, the incident electromagnetic wave excites current in the plasma, which is re-radiated at the same frequency. Many of these weak individual reflections add constructively, resulting in a condition for strong constructive interference,

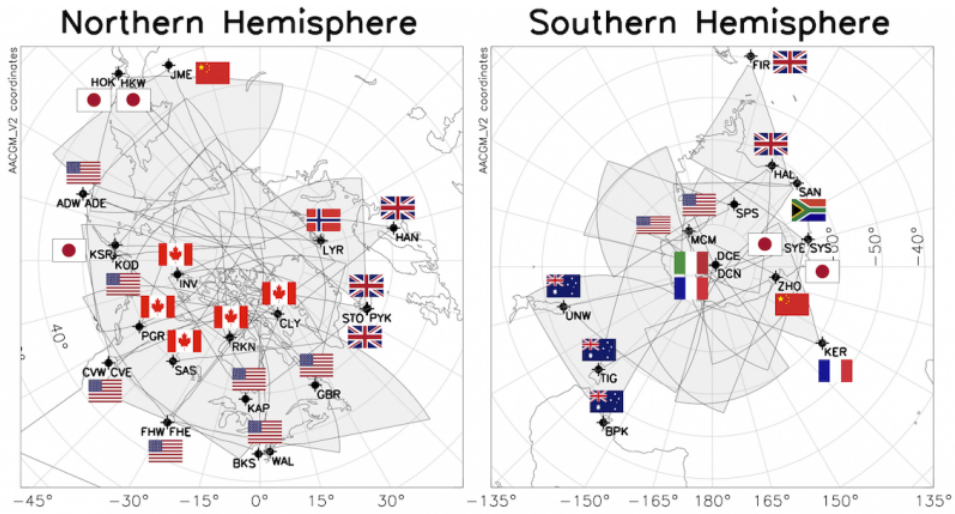

Figure 1.6: A coverage map of all SuperDARN radars currently in operation across the globe. Three letter radar codes are displayed, as well as the nations which operate them. Each radar's field-of-view is shown. Radars cover regions of polar, high, and mid-latitudes. Many areas feature overlapping coverage.

known as Bragg scattering. However, the irregularities are magnetic field aligned and the geometry requires the incident wave Poynting vector to be perpendicular to the background magnetic field. As with other forms of radar backscatter, this technique allows for Doppler measurements which provide LOS velocity information. However, unlike most radars, the intended targets are "soft", meaning the signal must be allowed to propagate through a significant volume in order to aggregate enough returned power to make measurements. An analogous radar system would be a weather radar, which needs to travel through a volume of rain. However, not all returns come from these soft plasma irregularities, and most returns are actually from the ground. Radar signals reaching back to the ground are possible as SuperDARN is designed to operate at a frequency slightly above the foF2. This causes refraction of the rays as they get to regions of higher refractive index. These rays can bend over themselves, and back towards the ground at ranger further than the horizon. In fact, SuperDARN rays have been known to produce returns from two and even three so called "hops". This SuperDARN ray behavior is shown in Figure 1.7. This figure also

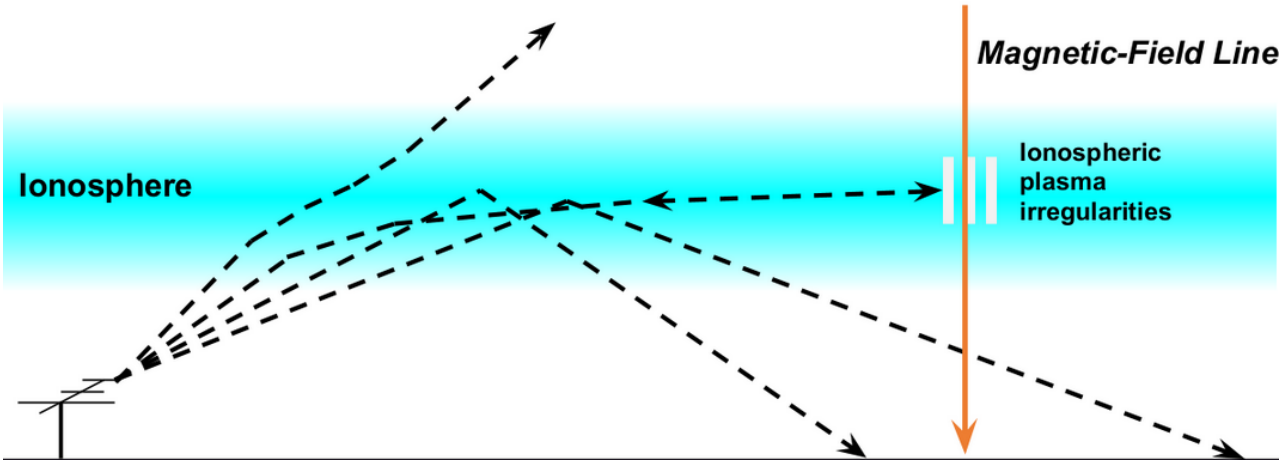

Figure 1.7: Ray-tracing drawing of a SuperDARN HF radar. Rays originating from different elevation angles take various paths through the ionosphere. Some rays bend back towards the ground, where they are reflected. Others pass entirely through the ionosphere to space. In between these two scenarios, rays which encounter plasma irregularities at orthogonal conditions are scattered back to the radar.

demonstrates the importance of choosing a frequency based on ionospheric conditions. If the frequency was too high, all rays would pass through the ionosphere. Meanwhile, at too low a frequency, all rays would bounce back to earth before encountering field aligned irregularities. Typically, lower frequencies are chosen at night, as peak plasma density, and therefore foF2 is lower. However, Figure 1.7 does not show the consequences of the extreme range of the radars. Across a range of over 2000km, the curvature of the earth, variability of magnetic field lines, and variability of ionospheric conditions need to be accounted for. For example, a North-Westward pointing radar beam may see the mid-latitude day-side at near ranges and the high latitude night-side at further ranges. Field lines will also be more vertical at higher latitudes. Ideally, SuperDARN rays maximise the possibility for sensing plasma irregularities, based on plasma density and field line geometry. However, radars typically choose their own frequencies with limitations on usable spectrum due to communications.

SuperDARN radars operate in a linear phased array configuration. In this format, beam forming is accomplished using electronic phase delays. This allows for a 3.25° beam to

be steered across an azimuthal range of 52°. Early SuperDARN radars use log-periodic style antennas, while newer radars typically feature twin terminated folded dipole antennas (Sterne et al., 2011). One consequence of the radar beam forming technique is the beam cone effect (André et al., 1998), whereby radar beams at the azimuthal extremes see their azimuth increase with elevation angle. Therefore, a beam forms a "cone" in elevation and azimuth about the linear array. The consequence of this is some uncertainty of geo-location of returns from these azimuthal beams.

Radars use a pulse sequence to determine range. A unique pulse pattern of many pulses is transmitted over a 100 ms time period. Each individual pulse is 300 microseconds long, allowing for a maximum range resolution of 45km. An Auto Correlation Function (ACF) of the returns is produced to allow for range to be determined. Using this technique, returns are classified into 45km range gates. Radars usually feature 16 active antennas in a main array, as well as 4 receive only antennas in a supplementary interferometry array, typically located 100m behind the main array. The purpose of this second array is to detect the elevation of radar returns, using time-domain interferometry (André et al., 1998). SuperDARN radars operate across 8-20 MHz. Because of HF operation, the antenna arrays are physically large. To demonstrate this, an areal image of the Fort Hays radar is shown in Figure 1.8.

SuperDARN radars operate at relatively low power levels, peaking around 500-800 Watts for each active antenna. A typical duty cycle is less than 6%, meaning that the entire radar consumes less than 2kW of power. Because of this, SuperDARN radars are much lower cost to operate than alternatives, such as satellite based sensors or incoherent scatter radars. Besides occasional maintenance visits, SuperDARN radars do not require constant monitoring by operators. Many institutions across the world operate SuperDARN radars. Some radars, such as Fort Hays, Christmas Valley, and Hokkaido, use a dual configuration, whereby two radars are co-located at a site and scan twice the azimuthal range as a single

Figure 1.8: A photograph taken from an aircraft showing the layout of the Fort Hays, Kansas SuperDARN radar. The image was taken from the front of the radar looking southwards, with the interferometry arrays visible 100m behind the main arrays. The site features two radars, which view different azimuthal regions. The poles visible are the aluminum support structures which the wire antennas are mounted on. A control building, which houses radar electronics, is in the center.

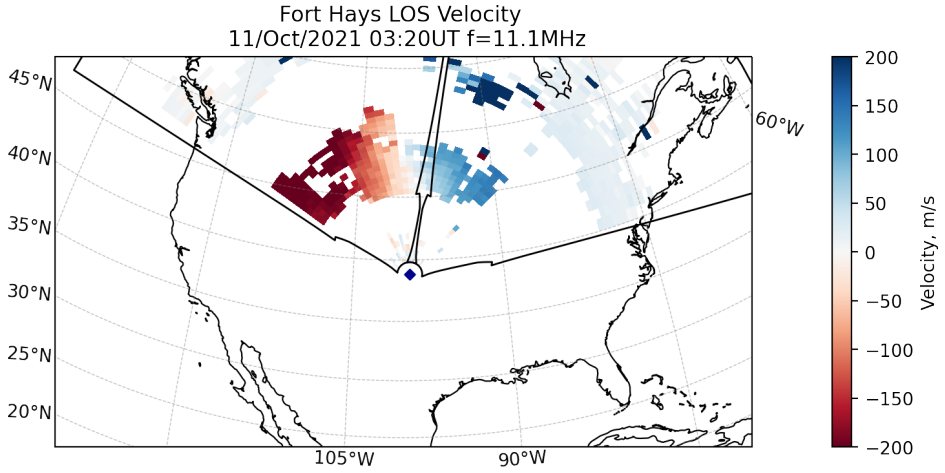

Figure 1.9: Example of SuperDARN fan plots. These plots use all beams of the radars at one time. This scan's time was 03:20UT on October 11th, 2021. Both Fort Hays West (left side) and East (right side) are shown. (This is the same set of radars shown in Figure 1.8).

radar. Other radars function effectively as a dual pair. For example, Wallops and Blackstone are located within 250km of each other, yet scan across different regions. All SuperDARN institutions share data with one another, allowing for widespread use of data.

SuperDARN data is available in various formats. The most basic of these is the raw in-phase and quadrature samples, known as an IQDAT file. ACFs are then used to calculate data parameters as a function of slant range. These files, called FITACF, are the primary analysis tool used for SuperDARN studies, including in this work. FITACF files contain data from an individual radar from a few hours. Radars scan across each of 16-24 beams typically over a one to two minute time period. Each of these scans can be used to produce a fan plot, which shows beam and range for a single time. Examples are shown in Figure 1.9. Fan plots can be especially useful to show the dominant plasma motion via the LOS velocity gradient with respect to azimuth. In the figure, a strong westwards velocity gradient is displayed. This would not be possible with a single beam. Fan plots are often used to show features at a single time, such as live maps of radar data and plasma motion.

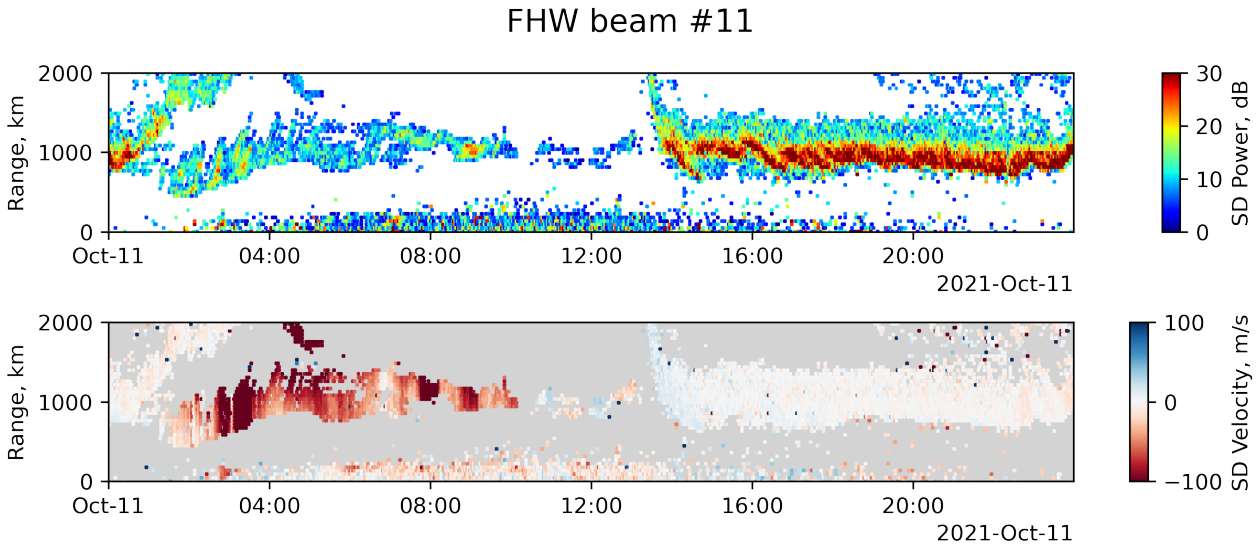

Figure 1.10: An example of an RTI plot. This plot covers the entire day for October 11th, 2021. Both power and LOS velocity are shown for beam 11 of the Fort Hays West radar (pictured in the right half of Figure 1.8). This is equivalent to plotting just one beam on a fan plot (Figure 1.9) through all scans of the whole day.

Using a single beam across a wide time period allows for a Range Time Intensity (RTI) plot, such as in Figure 1.10. This type of figure is often used to show features with long time periods. In this particular RTI plot, an entire day is covered. High velocity scatter is shown during local nighttime, indicated by deep red velocities. Later in the day, a TID is visible as oscillations in the power. This feature contains near-zero velocities, and is therefore likely due to AGW driving. RTI plots are also useful for features such as ULF waves and eclipses, where time is a significant factor. Fan plots and RTI plots are some of the most common plots generated with SuperDARN data.

Further accumulation of data across many radars allows for global convection mapping, using files known as GRID and MAP files. These files take into account all operating radars, and can be used to produce global maps of plasma convection. An example of this is shown in Figure 1.11. In this figure, all radars in the Northern Hemisphere have had their LOS velocity data aggregated. This global map of plasma convection is made using a few assumptions,

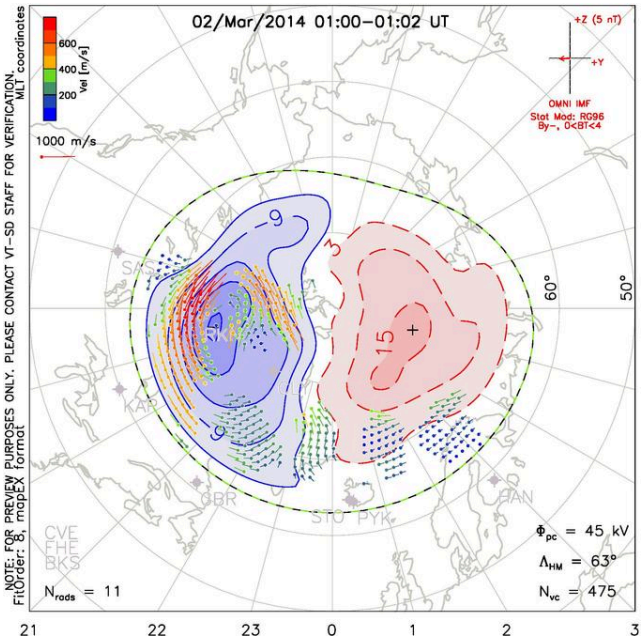

Figure 1.11: An example of a convection plot. This plot includes velocity vectors obtained from radar LOS velocity data. Additionally, this data has been used in line with magnetic field data to estimate electric potential in the ionosphere. Two cells of opposite polarity are visible spanning the polar cap of the Northern Hemisphere.

including a divergence free condition. Based on the $E \times B$ convention, electric fields can be estimated, since both velocity and magnetic field are known. Ruohoniemi and Baker (1998) describes the process for fitting all available velocity data into these global convection maps.

1.4.3 TIDs in SuperDARN

SuperDARN has been used to study TIDs since (Samson et al., 1990). SuperDARN has been used to show that AGWs are common at high latitudes and are caused primarily by auroral sources from space weather (Samson et al., 1990; Bristow et al., 1994, 1996). Frissell et al. (2014) examined the climatology of MSTIDs, restricted to AGWs. This work found that mid-latitude MSTIDs occur most often in North America during winter months. Frissell et al. (2016) analysed MSTIDs over North America using high and mid-latitude SuperDARN

radars. This study focused on day-side winter MSTIDs, which were assumed to be AGW driven. It found that MSTIDs were related to atmospheric processes such as the polar vortex, and not to space weather. In all these studies, the driver behind these TIDs was assumed to be gravity waves, regardless of whether TIDs were sourced from space weather or not. Under this assumption, the primary mechanism for SuperDARN observations of TIDs is the focusing and de-focusing of ground scatter signals. The ray-tracing basis for this approach is demonstrated in Figure 1.12. This effect is visible in the figure as lines of constant plasma density, which reveal a two dimensional slice of a TID. In this scenario, rays at different elevation angles reach different densities, and therefore refract through different angles. A density structure acts to lens the rays. Figure 1.10 shows an example of the result in an RTI plot format. The signature of the TID is seen as the wave structures visible in the power plot. One important feature of this regime is that returns originate from twice the range at which TID features are sensed. This means that a range translation is needed to accurately characterize the position of TIDs. Bristow et al. (1994) presents

$$D \approx R_e sin^{-1}\left(\frac{\sqrt{R^2/4 - h^2}}{R_e}\right)$$

as the equation for the ground scatter mapped range (D). R is the slant range, which is known from radar measurements. R_e is the radius of the Earth (6371km), and h is the height of the ionosphere (250-350km). The consequence of applying this equation is that TIDs occur at slightly less than half of the original observed range.

SuperDARN investigations of MSTIDs have also suggested that decameter-scale field aligned irregularities could also be a cause of TID observations. Ogawa et al. (2009) directly compares measurements from SuperDARN to TEC and airglow intensity. Notably, this study did not apply the ground scatter mapping function. Instead, plasma is directly sensed by the

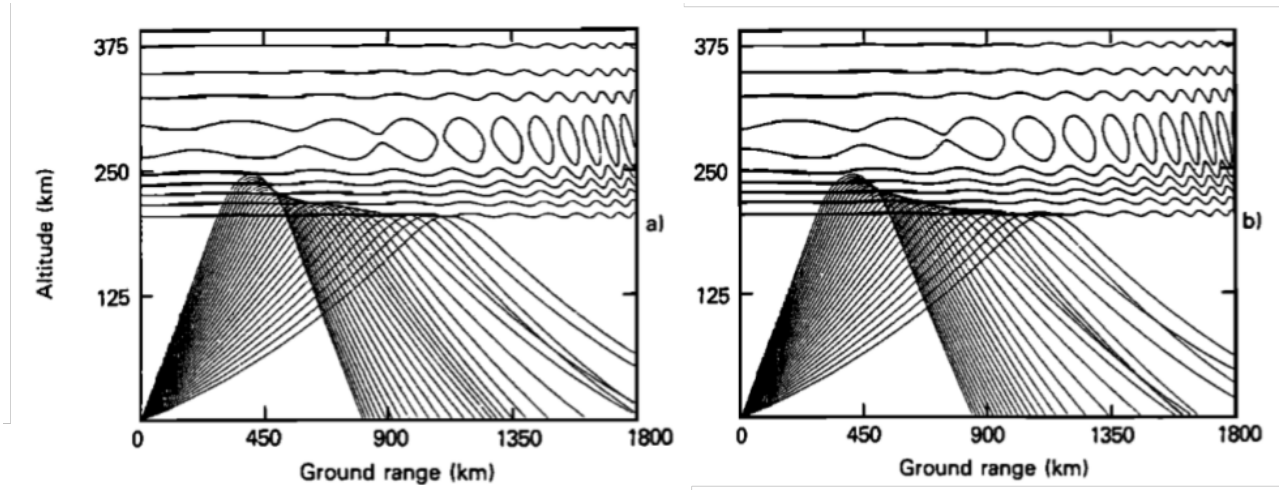

Figure 1.12: Ray paths of a SuperDARN radar are modulated by a TID. Rays focus and de-focus on areas of the ground as the TID propagates through the Ionosphere. (a) proceeds (b) by 15 minutes. This figure is taken from (Samson et al., 1990).

radars. This approach is also taken in other studies (e.g., Suzuki et al., 2009; Otsuka et al., 2009, 2013). In addition, these studies found that while AGW driven MSTIDs are observed in ground-based scatter, electrified MSTID observations come directly from ionospheric irregularities. Electrified MSTIDs will therefore be observed by SuperDARN as ionospheric scatter, with LOS velocity fluctuations in line with the motions of the density fluctuations of the MSTID.

Observations of AGW-driven MSTIDs will be due to ground scatter focusing, with little LOS velocity behavior. Because these features are located in the ionosphere, but captured in ground scatter, the ground scatter mapping equation needs to be applied. This allows for direct comparison of SuperDARN results to other datasets, such as GNSS TEC.

1.5 Scientific Objectives

Electrified MSTIDs have been shown in various observational techniques. They have been attributed to the Perkins instability (Perkins, 1973). Their theory has been refined (Kelley and Fukao, 1991; Garcia et al., 2000; Zhou and Mathews, 2006; Kelley, 2011) to address issues such as the growth rate and ionospheric conditions. Specifically, electrified MSTIDs have been shown to be more common at night, quiet times, and at mid-latitudes. E/F region coupling is an important factor behind the growth rate of these MSTIDs. Sporadic E has been suggested as a primary cause of these MSTID (Narayanan et al., 2018). Electrified MSTIDs fitting into this existing understanding have been shown using the Hokkaido SuperDARN radar (Ogawa et al., 2009; Suzuki et al., 2009; Hazeyama et al., 2022). In these studies, evidence for polarization electric fields is shown based on LOS plasma velocity fluctuations coinciding with MSTID density fluctuations. MSTIDs were observed directly as ionospheric radar scatter, as opposed to ground scatter focusing (e.g., Samson et al., 1990).

During an intense storm time event, on September 7th and 8th, 2017, Zhang et al. (2019) showed clear evidence of MSTIDs propagating westwards in the North American region during the storm peak. Based on the propagation direction, it was suggested that these MSTIDs were either electrified, or that they were AGW driven by supersonic (above 1km/s) westwards plasma flows. However, this point could not be resolved without measurements of internal electric fields within the MSTIDs. By taking an approach similar to (Ogawa et al., 2009) SuperDARN radars in mid-latitude North America can be used to determine the role of electrodynamic processes in driving the MSTIDs. This work concludes that the MSTIDs are indeed electrified, containing LOS plasma velocity fluctuations reaching $\pm$500 m/s, corresponding to electric fields of approximately $\pm$ 25 mV/m. These polarization electric fields are significant, and likely map along magnetic field lines.

1.6 Thesis Organization

This work is organized into three chapters. In Chapter 1, GNSS TEC, SuperDARN, and electrified MSTIDs have been introduced. In Chapter 2, the observations during an event are presented, and the above questions are answered. Using data from the September 7-8, 2017 storm interval, it can be concluded that the MSTIDs observed contain electrodynamic driving. Furthermore, this work presents a new type of MSTIDs, as storm time electrified MSTIDs have not been previously demonstrated. Chapter 2 has been submitted as a manuscript to the Journal of Geophysical Research: Space Physics, and is available as a pre-print at (Kelley et al., 2022). Finally, Chapter 3 summarizes this work and presents ideas for future work.

Chapter 2

Storm Time Electrified MSTIDs

I. J. Kelley[1], B. S. R. Kunduri[1], J. B. H. Baker[1], J. M. Ruohoniemi[1], and S. G. Shepherd[2]

[1]Bradley Department of Electrical and Computer Engineering, Virginia Tech, Blacksburg, Virginia, USA.

[2]Thayer School of Engineering, Dartmouth College, Hanover, NH, USA

Manuscript submitted to Journal of Geophysical Research: Space Physics on July 12th, 2022.

2.1 Abstract

edium-scale Traveling Ionospheric Disturbances (MSTIDs) are prominent and ubiquitous features of the mid-latitude ionosphere, and are observed in Super Dual Auroral Radar Network (SuperDARN) and high-resolution Global Navigational Satellite Service (GNSS) Total Electron Content (TEC) data. The mechanisms driving these MSTIDs are an open area of research, especially during geomagnetic storms. Previous studies have demonstrated that night-side MSTIDs are associated with an electrodynamic instability mechanism like Perkins, especially during geomagnetically quiet conditions. However, day-side MSTIDs are often associated with atmospheric gravity waves. Very few studies have analyzed the mecha-

nisms driving MSTIDs during strong geomagnetic storms at mid-latitudes. Here, we present mid-latitude MSTIDs observed in de-trended GNSS TEC data and SuperDARN radars over the North American sector, during a geomagnetic storm (peak Kp reaching 9) on September 7-8, 2017. In SuperDARN, MSTIDs were observed in ionospheric backscatter with Line Of Sight (LOS) velocities exceeding 800 m/s. Additionally, radar LOS velocities oscillated with amplitudes reaching $\pm$500 m/s as the MSTIDs passed through the fields-of-view. In detrended TEC, these MSTIDs produced perturbations reaching $\sim$50 percent of background TEC magnitude. The MSTIDs were observed to propagate in the westward/south-westward direction with a time period of $\sim$15 minutes. Projecting de-trended GNSS TEC data along SuperDARN beams showed that enhancements in TEC were correlated with enhancements in SuperDARN SNR and positive LOS velocities. Finally, SuperDARN LOS velocities systematically switched polarities between the crests and the troughs of the MSTIDs, indicating the presence of polarization electric fields and an electrodynamic instability process during these MSTIDs.

2.2 Introduction

Traveling Ionospheric Disturbances (TIDs) (Munro, 1948) are wave-like structures which propagate through the ionosphere. TIDs are most commonly expected to be driven by Atmospheric Gravity Waves (AGWs) originating in the neutral atmosphere (Hines, 1960) and can be sensed with instruments used for monitoring ionospheric dynamics such as Global Navigational Satellite Service (GNSS) Total Electron Content (TEC) (Saito et al., 1998) and coherent scatter radars (Samson et al., 1990; Fukao et al., 1991). TIDs are further classified as either Large-Scale (LSTIDs) or Medium-Scale (MSTIDs) based on their spatio-temporal scales (Georges, 1968). MSTIDs typically have a time-period of 15-60 minutes, phase velocities of 100-300 m/s, and wavelengths between 200-800km. On the other hand LSTIDs have phase speeds between 400-1000 m/s, periods above 30 minutes, and wavelengths above 1000 km (Hocke and Schlegel, 1996; Hunsucker, 1982). The differences between MSTIDs and LSTIDs are not just limited to their spatio-temporal scales, previous studies have shown that the underlying generation mechanisms and the physics of their propagation also differ (Hocke and Schlegel, 1996). MSTIDs are often linked to Atmospheric Gravity Waves (AGWs), which are a neutral atmospheric phenomenon generally carrying more energy than the TIDs themselves (Hunsucker, 1982). Such AGW-driven MSTIDs are more commonly reported at high latitudes, and on the day-side, and in the winter (Bristow et al., 1994; Frissell et al., 2014). The AGWs are in turn expected to be driven by factors such as tropospheric weather (Chou et al., 2017), Joule heating (Chimonas and Hines, 1970), and ground-based disturbances including tsunamis and earthquakes (Liu et al., 2011). Determining the sources of AGWs/MSTIDs can be challenging since they travel thousands of kilometers from the source and dissipate along the propagation paths (e.g., Vadas, 2007; Ogawa et al., 2009). Previous studies have demonstrated the utility of SuperDARN for analyzing MSTIDs (e.g., Samson et al., 1990; Bristow et al., 1994; Grocott et al., 2013; Frissell et al., 2014). In particular,

these studies have shown that quasiperiodic density rarefactions and enhancements in ionospheric layers produced by MSTIDs manifest as moving bands of enhanced ground scatter power in SuperDARN observations.

In addition to AGWs, MSTIDs have also been associated with electrodynamic instabilities (Perkins, 1973; Miller, 1997). Such MSTIDs are linked to perturbations and oscillations in electric fields (e.g., Shiokawa et al., 2003; Otsuka et al., 2004, 2007; Suzuki et al., 2009). A few studies showed that these electrodynamic instabilities can map into the other hemisphere along magnetic field lines and drive MSTIDs in the conjugate location (Otsuka et al., 2004; Valladares and Sheehan, 2016). Electrified MSTIDs exhibit properities that are different from those linked to AGWs. Specifically, electrified MSTIDs were frequently observed on the night-side, propagating southwestwards. A majority of previous studies have reported electrified MSTIDs during quiet geomagnetic conditions and in summer months (Ogawa et al., 2009; Duly et al., 2013; Huang et al., 2016). Electrified MSTIDs are an active area of research and the mechanisms seeding the instability processes are yet to be fully understood. For example, it has been shown that the growth rate of the instability alone is not sufficient to seed nighttime MSTIDs (Garcia et al., 2000), and coupling with the E-region and sporadic-E instabilities can re-inforce the process (Otsuka et al., 2007; Ogawa et al., 2009). A few previous studies have used measurements from airglow imagers or TEC in combination with SuperDARN observations of electric fields to analyze the behavior and characteristics of electrified MSTIDs during geomagnetically quiet conditions (e.g., Ogawa et al., 2009; Suzuki et al., 2009). Two main features were reported by these studies. First, the Doppler Line of Sight (LOS) velocities switched polarities as the crests and troughs associated with the MSTIDs passed through the radar's field-of-view. Secondly, depletions in airglow intensity and TEC were correlated with enhancements in SuperDARN ionospheric backscatter power.

Geomagnetic storms have often been shown to drive significant LSTID activity (e.g. Ding

et al., 2007; Borries et al., 2009). However, very few studies have reported and analyzed storm-time MSTIDs (e.g., Zhang et al., 2019). Such disturbed intervals can be challenging to analyze since several different factors such as neutral winds, Sub-Auroral Polarization Streams (SAPS), and strong ion-neutral coupling can be active simultaneously (Guo et al., 2018; Zhang et al., 2019), especially at mid-latitudes. For example, Guo et al. (2018) suggested that thermospheric heating by SAPS electric fields can induce regional disturbances which manifest as AGWs and TIDs. In addition, changes in neutral winds induced by SAPS electric fields (e.g., Zhang et al., 2017b) can drive changes in the propagation of AGWs and associated TIDs. While Joule heating during geomagnetic storms is expected to drive AGWs and TIDs, a few studies have hypothesized the possibility that electrodynamic instabilities can also play a role (Zhang et al., 2019). Overall, there has been very limited focus on analyzing the role of electrodynamic instabilities in driving MSTIDs during geomagnetic storms.

In this study, US mid-latitude SuperDARN observations are used alongside high-resolution GNSS TEC data to analyze MSTID activity during a strong geomagnetic storm that took place on Sep 7-8, 2017. The MSTID characteristics (wavelength, time period, etc) are derived from these two datasets are compared. We determine that the MSTID activity in this event was associated with an electrodynamic instability.

2.3 Datasets

The Fort Hays, Kansas, and Christmas Valley, Oregon, mid-latitude SuperDARN radars are used to study the MSTIDs observed during this event. High-resolution GNSS TEC in the North American sector is used in conjunction with SuperDARN to characterize the MSTIDs. In this section, these datasets will be defined. Their coverage, techniques, and data will be

outlined in the following section. Additionally, datasets used for capturing geomagnetic indices will be defined.

2.3.1 SuperDARN

SuperDARN is a global network of High-Frequency (HF) radars covering polar, high, and mid-latitudes in both hemispheres (Greenwald et al., 1995; Chisham et al., 2007; Nishitani et al., 2019). SuperDARN radars observe coherent backscatter from decameter-scale irregularities aligned along the geomagnetic field. The Doppler velocity of the back-scattered signal is proportional to the LOS component of E $\times$ B plasma drift within the scattering region (Ruohoniemi et al., 1987). The radars electronically steer across different look directions. A radar typically scans through 16 beams in 1 minute, covering $\sim$50° of azimuth. The first SuperDARN radar came into operation at Goose Bay, Labrador (Canada) in 1983. Over the following decades many others were built to improve coverage across the high-latitude regions of both the Northern and Southern Hemispheres. The SuperDARN network later expanded to the mid-latitudes to enable observations of plasma convection during intervals of very strong geomagnetic activity when the auroral oval and convection extend equatorwards (Baker et al., 2007; Nishitani et al., 2019). The most commonly used SuperDARN parameters include power which is measured in dB of SNR above the noise floor, and LOS Doppler velocities.

2.3.2 GNSS Total Electron Content

Total Electron Content (TEC) is a columnar electron density measurement between a satellite and ground-based receiver. Using Global Navigational Satellite Service (GNSS) constellations allows for widespread TEC measurements across the globe. TEC is typically measured

in TEC units (TECu), where 1 TECu=$10^{16}\, electrons/m^2$. Worldwide GNSS TEC data is collected and processed at the MIT Haystack Observatory and available from the Madrigal database (http://www.openmadrigal.org) (Rideout and Coster, 2006; Vierinen et al., 2016). Several previous studies have shown the utility of GNSS TEC data for monitoring and analyzing MSTIDs over large geographical regions (e.g., Tsugawa et al., 2007; Zhang et al., 2017a, 2019). Data is available at 30 second time cadence, which is more than sufficient for observing MSTID activity (Saito et al., 1998). Each LOS GNSS TEC data point contains satellite, receiver, latitude, longitude, elevation angle, and timestamp, along with the TEC value. Both the American GPS constellation and Russian GLONASS constellation are sources of data in this study. All data points with low elevation angles ($< 30^\circ$ between ray-path and horizon) have been discarded to increase confidence in the measurements. Additionally, vertical TEC values were derived by accounting for the elevation angles. The TEC data from each satellite-receiver pair is de-trended by subtracting a rolling average over a 30-minute sliding window. This approach is similar to the methods discussed in Zhang et al. (2017a) and Lyons et al. (2019), and preferentially selects TIDs with periods less than 30 minutes. High frequency components/noise were not filtered out in this approach. MSTIDs during this event were large in amplitude and prominent, so TEC data processing is not as consequential as compared to geomagnetically quiet intervals when perturbations in TEC are smaller.

2.3.3 Solar wind, IMF and geomagnetic indices

In the current study, 1-min averaged OMNI values (King and Papitashvili, 2005), time shifted to the bow shock sub-solar point were used to examine the Interplanetary Magnetic Field (IMF) and solar wind conditions. The impact of geomagnetic disturbances on mid-latitudes electrodynamics were examined using the asymmetric (Asym-H) and symmetric

(Sym-H) disturbance indices (Iyemori, 1990). Note that the Sym-H and Asym-H indices have a temporal resolution of 1-minute. Finally, the impact of auroral electrojets during the event was analyzed using the AL and AU indices (Davis and Sugiura, 1966).

2.4 Results

2.4.1 Event Overview

The event analyzed in this study occurred during the main phase of a major geomagnetic storm on Sep 7-8, 2017. Kp reached a peak of 9 at ∼1:30 UT on September 8th, 2017. An overview of the geomagnetic conditions over a 48-hour interval is presented in Figure 2.1. From top to bottom, the figure presents IMF Bz and By components, solar wind velocty (Vx) and number density, AL and AU indices, and Sym-H and Asy-H indices. The specific period of interest for this study is highlighted in the figure as the time interval between 23 UT on Sep 7, 2017 and 2 UT on Sep 8, 2017. It can be noted that IMF Bz turns sharply negative at ∼23:00 UT on the 7th, dropping to ∼-30 nT by 0:00 UT on the 8th. Around the same time, solar wind velocity increases from km/s to 700 km/s along with multiple upturns in number density. We note that the Sym-H index drops to ∼-200 nT during the interval of interest, marking the main phase of the geomagnetic storm. Finally, elevated AL magnitude (∼-2500 nT) and upticks in the Asy-H index (reaching 250 nT) are indicative of strong substorm activity and enhancement of the partial ring current. Overall, MSTIDs analyzed in this study occurred during an interval of strong geomagnetic driving when SAPS is expected to dominate the sub-auroral ionosphere with velocities reaching several hundred m/s (Kunduri et al., 2018; Zhang et al., 2019).

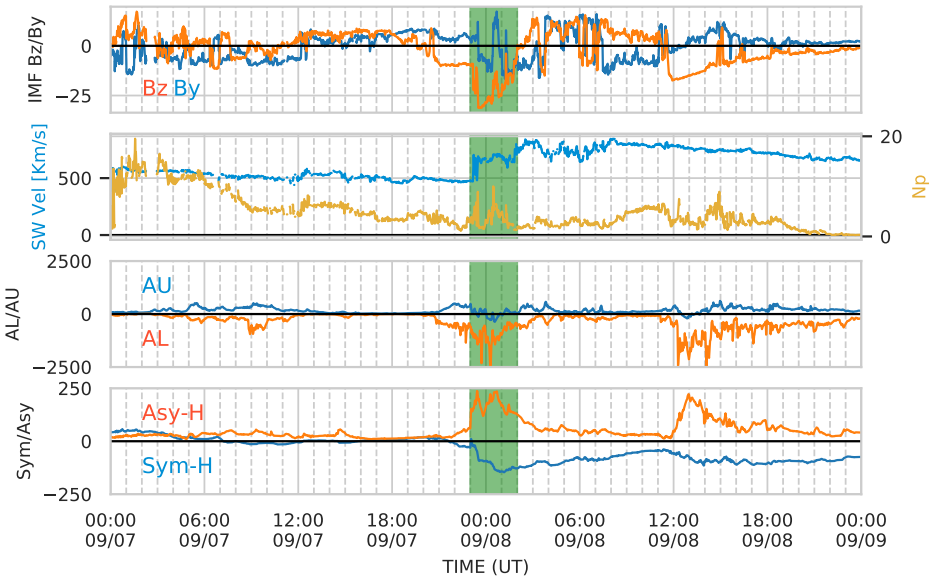

Figure 2.1: An overview of the geomagnetic conditions on September 7th and 8th, 2017. The conditions are shown over a 48 hour window, with the relevant time period for this study highlighted in green. The top two panels show IMF Bz/By, solar wind speed and density from the OMNI dataset. Third panel shows the auroral electrojet indices AU and AL, and the fourth panel shows the Sym-H/Asy-H indices.

2.4.2 GNSS TEC Observations

A snapshot of raw and de-trended GNSS TEC measurements during the main phase of the storm at 0 UT on Sep 8, 2017 is presented in Figure 2.2. The top panel of the figure shows raw TEC measurements over the North American continent and the bottom panel show the 30-minute de-trended TEC, scaled according to the color bar on the right. The outlines of Christmas Valley East beam 18, Fort Hays West beam 18, and Fort Hays East beam 14 are overlaid in the top-panel to provide context when comparing TEC measurements with SuperDARN in later sections. The de-trended TEC data shows a complex TID pattern including both LSTIDs and MSTIDs. The focus of this study is the MSTID activity observed in the north-central United States, centered around 45°N, 95°W (see region outlined in Figure 2.2.b). For reference, this location is about 150km west of Minneapolis, Minnesota. An important feature is that the MSTIDs are collocated with a trough-like feature observed in raw TEC data. A previous study (Zhang et al., 2019) reported observations of SAPS by the Millstone Hill ISR during the event, suggesting these MSTIDs could be linked to SAPS flows. The MSTID phase fronts are oriented North-Northwest to South-Southeast, suggesting that the direction of propagation is West-Southwest.

The propagation direction is shown in Figure 2.3 which displays de-trended TEC as a function of latitude vs UT (top panel) and longitude vs UT (bottom panel). This figure considers the de-trended TEC sampled geographically within the region of between 43-47°N and 108-112°W. As the sampled region is small relative to the MSTID structures, the latitude and longitude plots appear similar. The sampled region for Figure 2.3 is in the Western portion of the the red highlighted area in Figure 2.2. The perturbations in de-trended TEC are particularly strong, reaching an amplitude of ±4 TECu which forms a significant proportion of the background TEC, which varies between 10-20 TECu. In Figure 2.3.a, a slight equatorwards component can be detected. The Westwards velocity component (∼1 degree per

minute) is stronger than the Southward component. The period of the MSTIDs are consistent between both plots. This period varies from ∼7-20 minutes throughout the interval from 0 UT to 2 UT. In the next sections, the perturbations in de-trended TEC will be compared with SuperDARN observations and the role of different factors such as electric fields in driving these MSTIDs will be analyzed.

2.4.3 SuperDARN Observations

The US mid-latitude SuperDARN radars were making measurements over the North American sector during the event. Of particular interest are the Christmas Valley East (CVE), Christmas Valley West (CVW), Fort Hays East (FHE), and Fort Hays West (FHW) radars. Fields-of-view of these radars cover the region where MSTIDs were observed in GNSS TEC. A snapshot of the measurements from the FHE and FHW radars at 0 UT on Sep 8, 2017 (same time presented in Figure 2.2) is shown in Figure 2.4. The top panel shows the LOS velocities observed by the radars and the bottom panel shows the power, scaled according to the color bar on the right. The red outline in the bottom panel marks the same region outlined in Figure 2.2 where MSTID activity was observed. We can note that SuperDARN backscatter power exhibits zonal variability, alternating between high and low-powered regions. It can also be noted that the radars were observing ionospheric backscatter with LOS speeds reaching 1 km/s. Another feature that stands out is the systematic transition from positive LOS velocities (blue colored) in FHE to negative LOS velocities (red colored) in FHW. This behavior suggests that the background plasma convection in the region is predominantly westwards. Multiple US mid-latitude SuperDARN radars observed strong ionospheric backscatter with LOS speeds reaching 1 km/s in the region where MSTIDs were observed in GNSS TEC data.

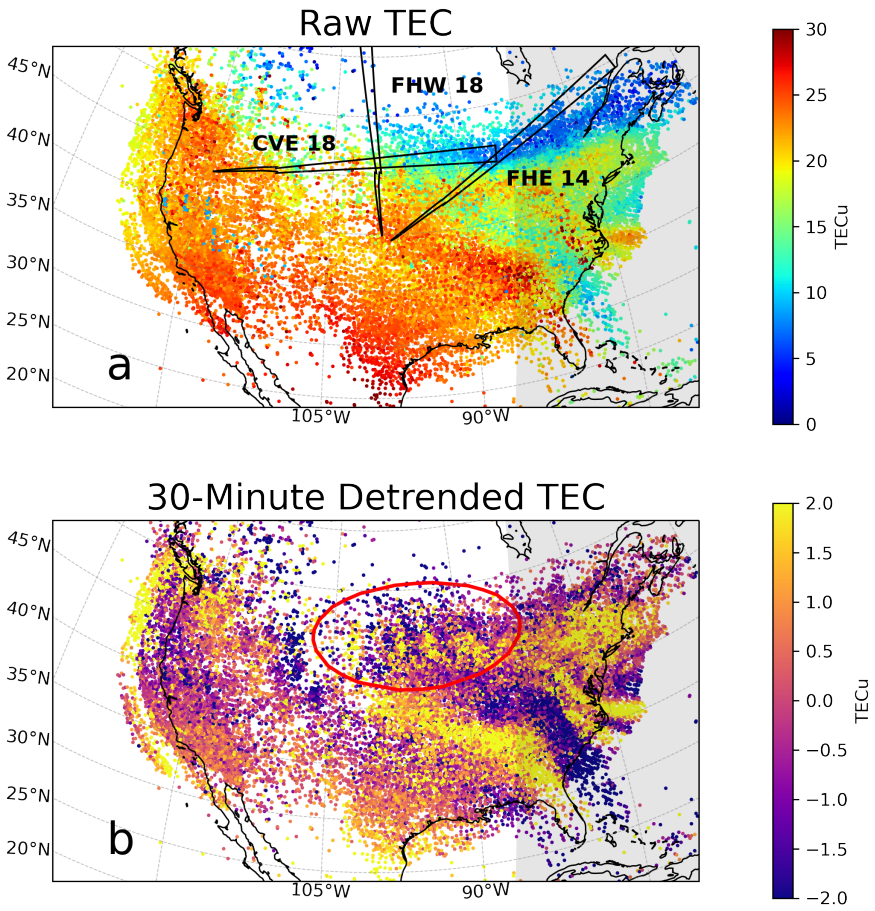

Figure 2.2: GNSS TEC observations over the North American sector on Sep 8, 2017 at 0:00 UT. Panel (a) shows raw TEC measurements. The outlines of Christmas Valley East radar beam 18, Fort Hays West radar beam 18, and Fort Hays East radar beam 14 are also overlaid on the map. Panel (b) shows 30-minute detrended TEC and the red outline indicates the region of interest with clear MSTID signatures. The grey shaded region denotes the day-night terminator.

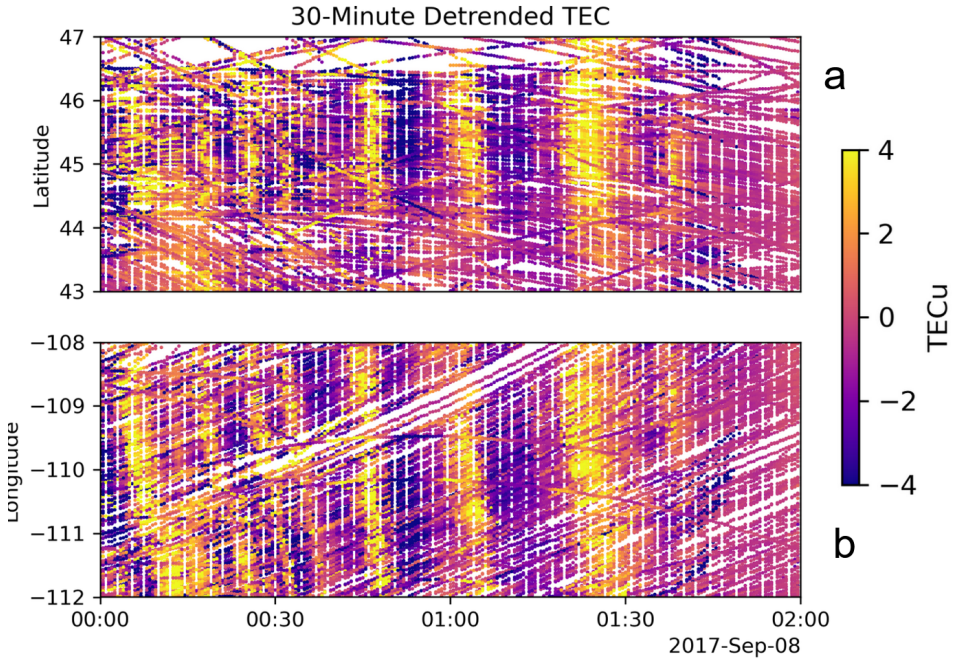

Figure 2.3: Spatio-temporal variability from TEC sampled with a limited 4x4 degree area. (a) shows de-trended TEC plotted as a function of latitude and UT plot and (b) shows de-trended TEC as a function of longitude and UT. TEC data for this plot is taken between 43-47°N and 108-112°W which corresponds to approximately 800km in slant range on Christmas Valley East beam 18.

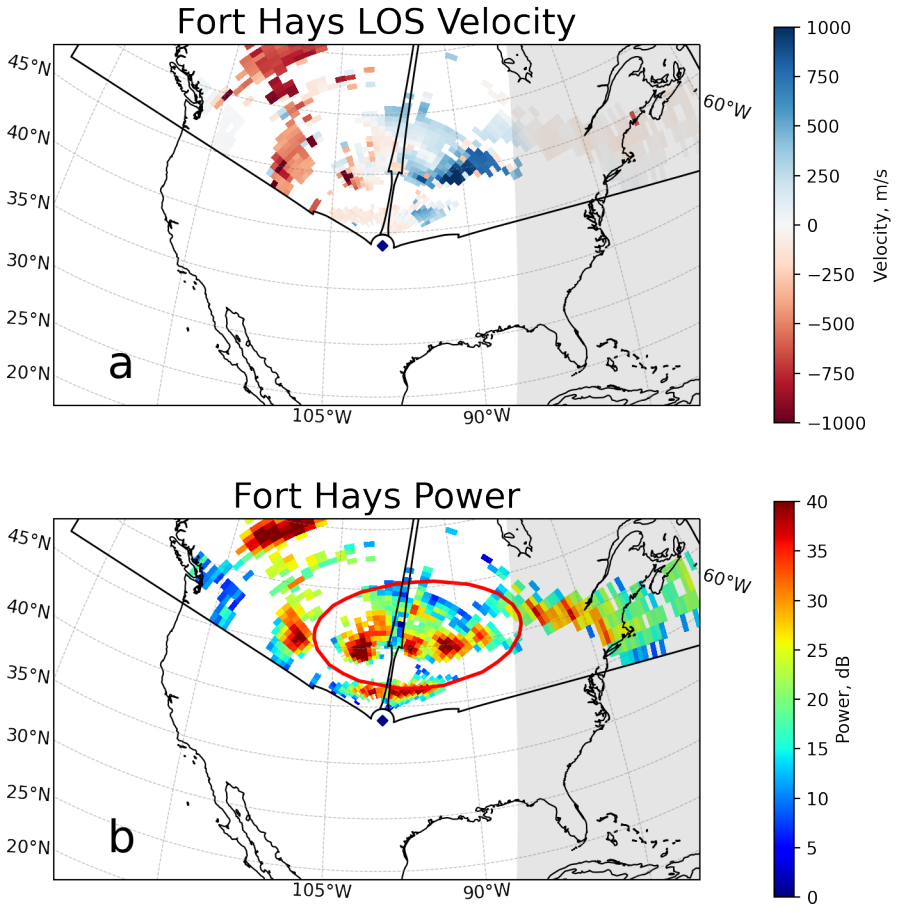

Figure 2.4: FHE and FHW radar measurements at 0:00UT on September 8th, 2017 (same time as Figure 2.2). Panel (a) presents SuperDARN LOS velocities scaled according to the color bar on the right. Panel (b) shows the SuperDARN backscatter power. The grey shaded region indicates the day-night terminator.

2.4.4 Comparison Between SuperDARN and GNSS TEC Observations

Projecting high-resolution GNSS TEC data along SuperDARN beams allows for direct comparison of the spatio-temporal variability observed in both datasets. GNSS TEC data is assumed to be sourced from a single pierce-point, which can be mapped within a given radar beam's footprint, with associated slant range and time. Note that the slant range for GNSS TEC is not limited to 45km bins as would be the case for SuperDARN data, and instead can be considered a continuous measurement. Similarly, the high-resolution GNSS TEC data has a 30 second time cadence, which is twice as fast as SuperDARN data which takes 1-2 minutes to complete a full scan across all beams. Despite the differences in the spatial and temporal resolutions of these datasets, this technique enables a direct comparison between observations made by a specific radar beam and the GNSS TEC within that beam. Figure 2.5 demonstrates a comparison along beam 18 of the CVE radar (left most beam marked Figure 2.2.a). Panel (a) of the figure presents de-trended TEC data projected along the beam, panel (b) presents the backscatter power observed on the beam, and panel (c) shows both the overlaid on top of each other. Similar to the observations presented in Figure 2.2 strong perturbations can be clearly noted from panel (a) starting ∼2330 UT on Sep 7 and continuing until 2 UT on Sep 8. A very similar "striation" in SuperDARN power can be observed in panel (b) with enhancements in backscatter power reaching 40 dB. Another interesting feature is that the "striations" can be observed at both near (< 500 km) and far ranges (1000-1500 km), over a total span of almost 2000 km. Finally, panel (c) qualitatively shows that the positive perturbations (enhancements) in de-trended TEC align well with the enhancements in SuperDARN power. The relation between de-trended TEC and SuperDARN backscatter power is further investigated using a correlation analysis in Figure 2.6 which shows a time-series plot comparing de-trended TEC and SuperDARN power between

Table 2.1: MSTID Characteristics as Determined by SuperDARN and TEC

Characteristic	Value from SuperDARN (CVE 18)	Value from TEC
Wavelength	$600 - 800\ km$	$660\ km$
Phase Speed	$800 - 900\ m/s$	$800\ m/s$
Period	$10 - 20\ min$	$10 - 20\ min$

300-600 km and 0045 and 0200 UT (marked in Figure 2.5). This range-time interval is chosen because of the absence of data gaps in both datasets. In this period, peaks in SuperDARN power align well the peaks in de-trended TEC, especially between 0100 and 0130 UT. A direct correlation between the two datasts is difficult due to the differences in temporal resolutions between them and moreover, TECu is a linear unit whereas dB (SuperDARN power) is logarithmic. The 1D Pearson correlation coefficient calculated using a two minute rolling average over both the datasets was 0.29. The two datasets didn't exhibit a strong correlation, and the differences in the spatio-temporal cadence between the two datasets likely contributed to it. However, it can be qualitatively stated that the peaks in de-trended TEC aligned with enhancements in SuperDARN power. Additionally, an artifact of beam forming SuperDARN radars is that the farther beams off boresight will have non-constant azimuthal angles as elevation increases. This is known as the beam cone, and is described by (André et al., 1998). This means that it is possible that measurements by CVE beam 18 and FHE beam 18 specifically may be slightly shifted from their reported position. However, the scale sizes of the MSTIDs are larger than any potential shift due to the beam cone effect, and it will not have a significant impact on our results.

In Table 1, the characteristics of the MSTIDs estimated from both the datasets are summarized. Specifically, the wavelength, phase speed, and the time-period of the MSTIDs are presented. These values were estimated manually. MSTID period was estimated by calculating the time-interval between two phase fronts, while the phase speed was estimated by calculating the slope of the striations. The process is illustrated in Figure 2.5.b, where phase

fronts are indicated by black lines. Beams that have a more zonal look direction are more suitable for this analysis (such as CVE beam 18 shown in the figure), since they are oriented more along the MSTID propagation direction. Note that the phase speed is different from the LOS velocities measured by SuperDARN radar. Values from SuperDARN radars show wavelengths between 500 and 1000 km, phase speeds of 800-900 m/s (LOS), and a time-period of 10-20 minutes. TEC estimates of these characteristics are in agreement. Estimates vary significantly through the event interval, as differing wave structures appear at different times. TEC estimates were made using Range-Time-Intensity (RTI) TEC plots (Figure 2.5), and keogram plots (Figure 2.3). Overall, despite the differences in spatio-temporal coverage between these two datasets, the characteristics of the MSTIDs estimated from them are largely consistent.

So far, the spatio-temporal variations in de-trended TEC and SuperDARN power have been compared and it was demonstrated that enhancements in TEC were collocated with enhancements in SuperDARN power. In Figure 2.7, a comparison between de-trended TEC and SuperDARN LOS vectors is presented along beam 14 of the FHE radar. In a format similar to Figure 2.5, panel (a) presents de-trended TEC, panel (b) shows LOS velocities along FHE beam 14, and panel (c) shows both the datasets overlaid on top of each other. Similar to the observations presented in Figure 2.5, strong perturbations in TEC can also be observed along this beam. Note that the color bar for SuperDARN LOS velocities shown in panel (b) is centered on 150 m/s to bring out the oscillations in velocities. It can be seen that the LOS velocities between 2330 UT and 0100 UT and 300-1200 km range oscillate around the central value with strong positive upswings collocated with enhancements in TEC. The polarity changes in SuperDARN LOS velocities become more evident in Figure 2.8 which is in the same format as Figure 2.7 but for beam 18 of the FHW radar, which is the poleward looking beam near mid-western United States (see Figure 2.2). (TEC coverage is sparse in

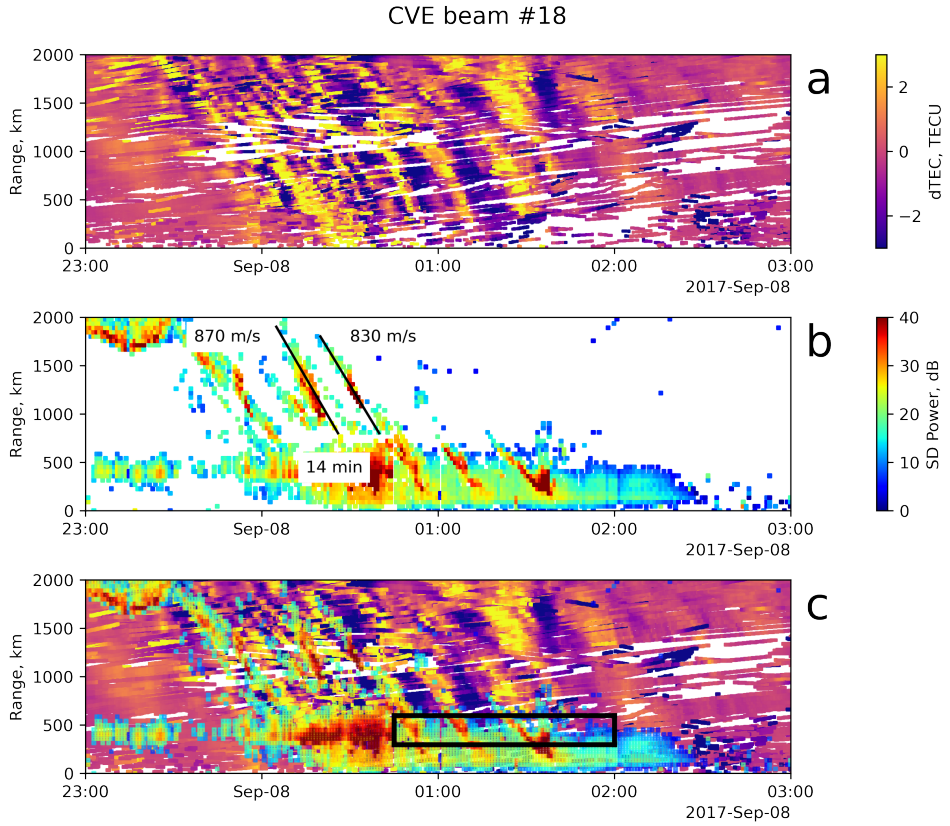

Figure 2.5: Comparison between SuperDARN and GNSS TEC measurements. Panel (a): de-trended GNSS TEC observations projected along CVE beam 18. Panel (b): CVE beam 18 measurements of backscatter power. Slope values allow for calculation of LOS phase speed. Panel (c) shows de-trended GNSS TEC from panel (a) and SuperDARN backscatter power from panel (b) overlaid on top of each other. The black boxed region contains data compared in 2.6.

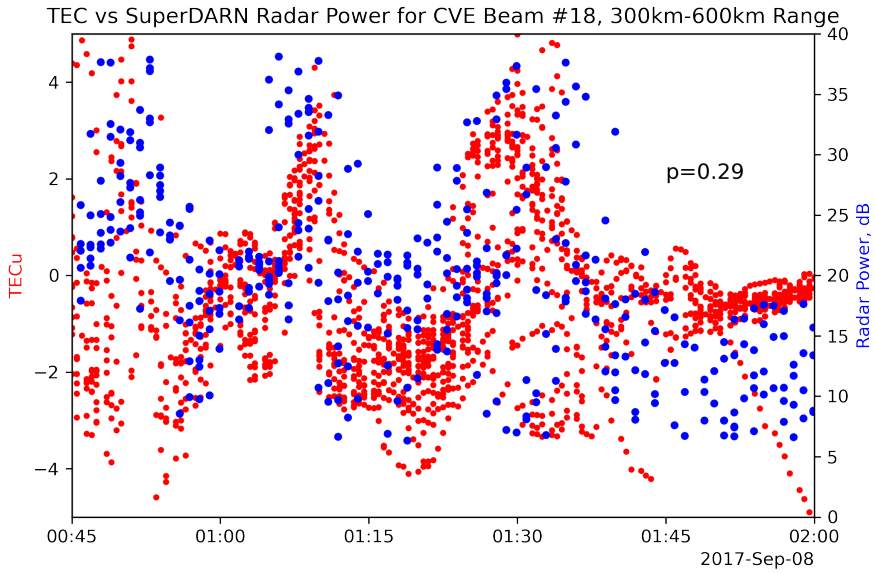

Figure 2.6: Time series plot showing correlation between maximum SuperDARN power level and mean detrended TEC. Data is taken between 300 and 600km along CVE Beam 18 shown in panel (c) of Figure 2.5. Rolling averages of the datasets are compared using a 1D Pearson correlation coefficient, resulting in p=0.29.

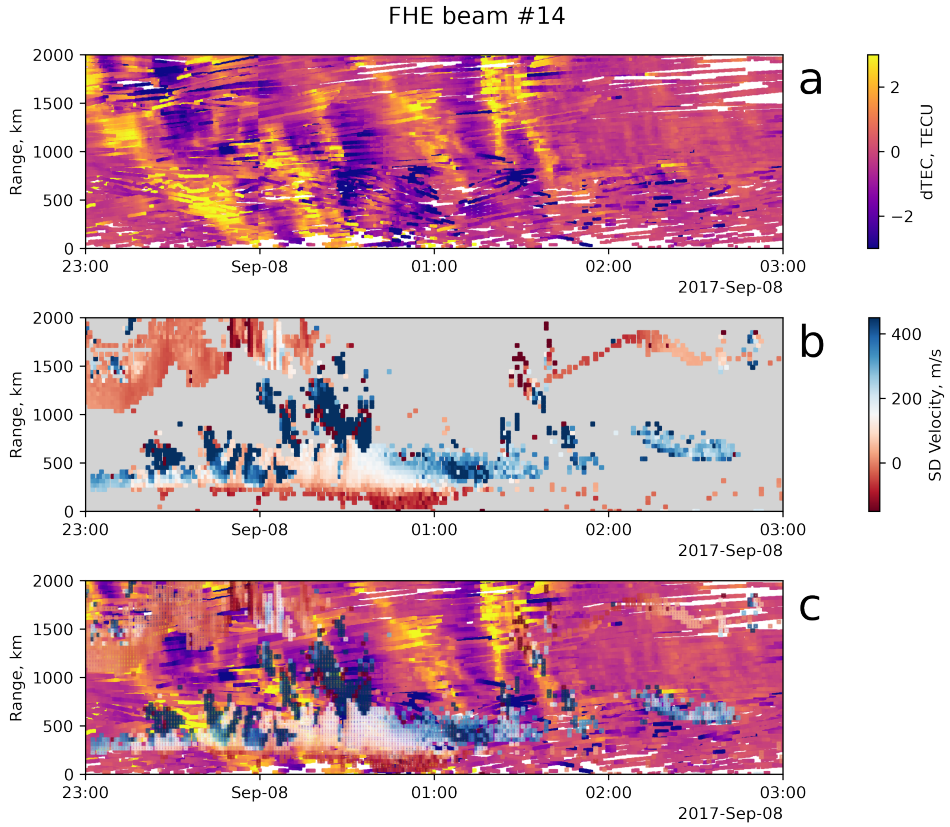

Figure 2.7: Comparison between SuperDARN LOS velocities and GNSS TEC measurements. Panel (a): de-trended GNSS TEC observations projected along FHE beam 14. Panel (b): FHE beam 14 measurements of LOS velocities. Panel (c) shows de-trended GNSS TEC from panel (a) and SuperDARN LOS velocities from panel (b) overlaid on top of each other.

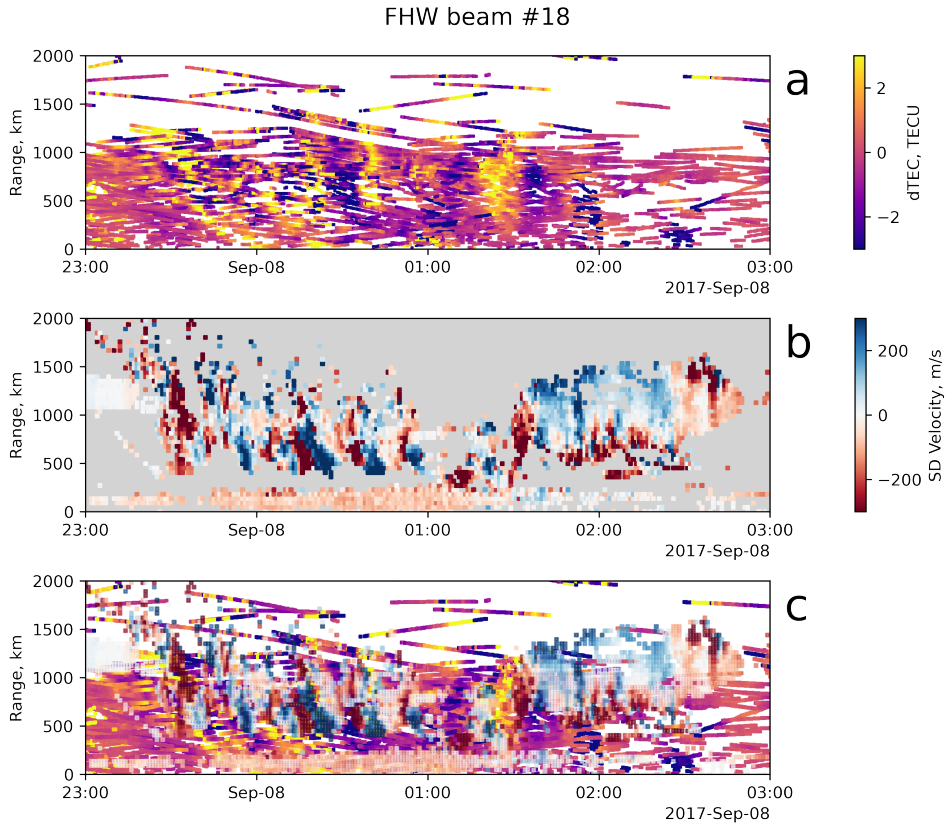

Figure 2.8: Same format as Figure 2.7 but for Fort Hays West Beam 18.

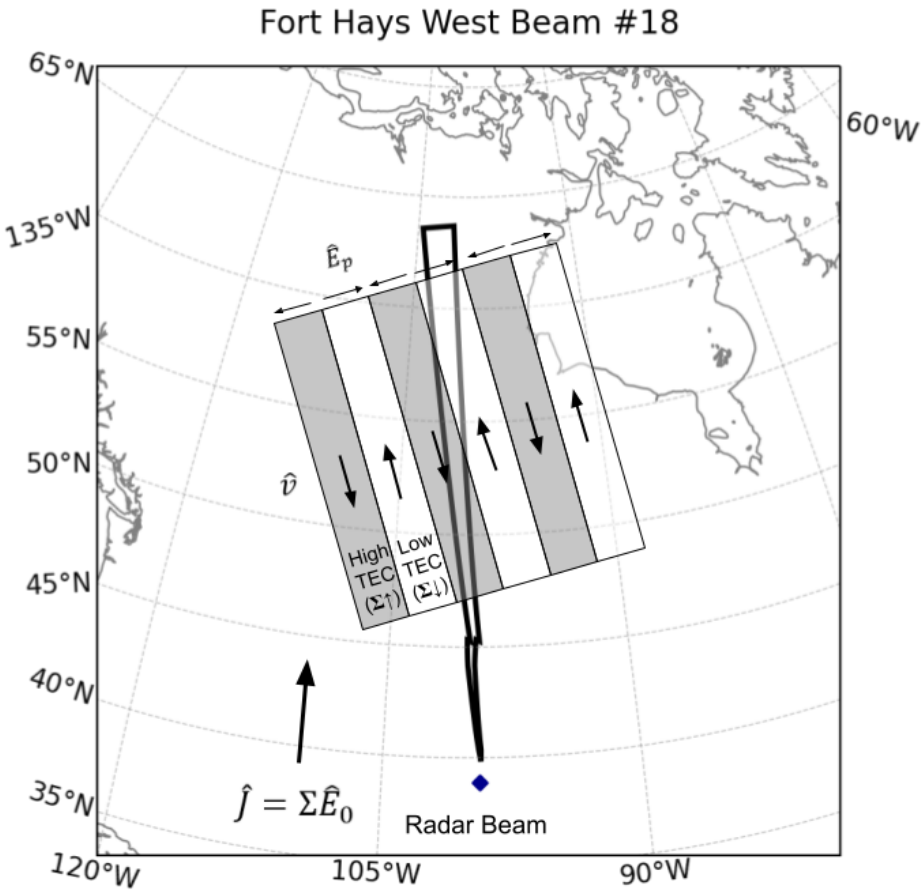

Figure 2.9: A schematic illustrating the proposed mechanism to explain the generation of polarization electric fields and their relation to MSTID wavefronts and background plasma convection. Polarization electric fields (E_P) are shown, as well as the resulting ExB drifts ($\hat{v}$).

the region which produces the data gaps in panel (a) of Figure 2.8.) The main feature that stands out from the figure is the systematic polarity change in LOS velocities as the MSTIDs pass through the beam. The color bar is now centered at 0, and velocities now oscillate with peak amplitudes exceeding ±300 m/s.

2.5 Discussion

In the previous sections, the characteristics of storm-time MSTIDs observed in high-resolution GNSS TEC and SuperDARN datasets were examined. Here, the current observations will be compared with those presented in previous studies, and the role of different factors in driving these storm-time MSTIDs will be determined.

An important feature from Figure 2.5 is that MSTID signatures in SuperDARN were observed in the near ranges (<500 km) as well as the farther ranges (∼1000-1500 km). Due to the nature of HF propagation, widley distributed backscatter from farther ranges is primarily due to F region irregularities, while backscatter from closer than about 600 km must be due to E region irregularities (Chisham et al., 2008). The transition in backscatter mode can be appreciated in Figure 2.5 with the change in backscatter characteristics that occurs at about 600 km. Here the intermittent backscatter at further ranges gives way to continuous backscatter over the E region ranges. While SuperDARN slant range can provide some additional context regarding the region of the ionosphere producing the backscatter, it is difficult to resolve altitude profiles of electron density using the GNSS TEC dataset. However, it is likely that a significant contribution to the variability observed in TEC is coming from the F region, where electron densities are expected to be the highest, even during geomagnetic storms (Hocke et al., 2019). A comparison between Figures 2.2 and 2.5 shows that the variability in TEC (indicated by dTEC) was very strong (∼50% of the background values),

suggesting that the F-region electron densities might be making significant contributions to the variability observed during this event. Overall, these observations from SuperDARN and GNSS TEC suggest that there was a strong coupling between the E and the F regions of the ionosphere during this event such that MSTID signatures are observed in both regions. This raises a key question: Do these MSTIDs originate in the E-region or the F-region? It is possible that Hall current driven processes generate polarization electric fields in the E-region which map into the F region and drive MSTIDs (Tsunoda and Cosgrove, 2001). It is also possible that E region echoes in SuperDARN are modulated by MSTIDs originating in the F-region. Previous studies have suggested that coupling between the E and the F regions and sporadic-E layers can augment and enhance the instabilities associated with MSTIDs (Otsuka et al., 2007; Ogawa et al., 2009). The Gradient Drift Instability (GDI) was suggested to be the primary plasma instability mechanism generating field-aligned irregularities observed by SuperDARN in such a case (Hiyadutuje et al., 2022). Regardless of the source region, it is clear that inter-region electrodynamics across altitude likely play a key role in furthering the plasma instability driving these storm time MSTIDs.

From Figure 2.1, it can be noted that the MSTIDs reported during this event were observed during the initial phases of a major geomagnetic storm. Zhang et al. (2019) analyzed the same event using the high-resolution GNSS TEC dataset and suggested two possibilities. The first is that ion-neutral frictional heating from the westward SAPS flows in the region produces AGWs and associated MSTIDs. Global Ionosphere-Thermosphere model (GITM) simualtions presented by Guo et al. (2018) showed that strong SAPS flows can significantly heat the thermosphere and drive TIDs. The second possibility is that polarization electric fields induced by an electrodynamic instability (e.g., Perkins, 1973) are driving the MSTIDs. It is not possible to determine if electrodynamic instabilities are driving the MSTIDs based soley on GNSS TEC data. Instead, additional measurements, such as those showing polariza-

tion electric fields, are needed. A few previous studies have shown that polarization electric fields, which systematically switch polarities between the crests and troughs in MSTIDs, manifest as oscillations in SuperDARN Doppler velocities (e.g., Ogawa et al., 2009; Suzuki et al., 2009). Such oscillations in the line-of-sight Doppler velocities are clearly evident during the current event, in beam 14 of the FHE (Figure 2.7) and beam 18 of the FHW (Figure 2.8) radars. The SuperDARN observations therefore confirm the presence of polarization electric fields during this event, and are in agreement with the conjecture made by Zhang et al. (2019) that these MSTIDs are driven by an electrodynamic instability. Finally, the south-westward propagation of MSTIDs observed during this event is similar to observations of electrified MSTIDs reported previously by Ogawa et al. (2009), which has been attributed to preferential Joule damping associated with electrodynamic instability processes (Kelley, 2011).

Previous studies have used mid-latitude SuperDARN observations in the Japanese sector to identify and analyze electrified MSTIDs driven by polarization electric fields (Ogawa et al., 2009; Suzuki et al., 2009). However, these reports focused on geomagnetically quiet intervals. Consequently, the main differentiating factor between the current observations and previous reports is the strong geomagnetic driving during this event (see Figure 2.1). We note from Figures 2.5, 2.7, and 2.8 that both the radar power and LOS velocity amplitude variations are almost an order of magnitude stronger than those reported previously. These differences are perhaps unsurprising, as this study is of an intense storm time event, and the mid-latitude electrodynamics are expected to be dominated by strong SAPS electric fields (Zhang et al., 2019). During geomagnetically quiet intervals, the mid-latitude electric fields are expected to be relatively weaker and driven by neutral winds (Suzuki et al., 2009). An examination of Figure 2.4 shows that the background plasma convection is predominantly westwards during the MSTIDs. The spatio-temporal relationship between SuperDARN LOS velocity and TEC

enhancements/depletions observed during the current event is different when compared to previous reports of quiet-time electrified MSTIDs (Otsuka et al., 2007, 2009; Suzuki et al., 2009). Specifically, enhancements in SuperDARN power during this event are aligned with enhancements in GNSS TEC (Figures 2.5 and 2.6), in contrast to quiet-time events where strong HF echoes were correlated with depletions in airglow/TEC (Otsuka et al., 2007, 2009; Suzuki et al., 2009; Ogawa et al., 2009). An interpretation of these observations is presented in Figure 2.9. The figure shows MSTID wavefronts passing through a poleward-directed radar beam. Regions of high TEC (conductivity) are shaded in dark. The directions of induced polarization electric fields (E_P) and the corresponding ExB drifts ($\hat{v}$) are marked in the figure. In the F-region, at mid-latitudes, the Pedersen current can be given as $J_P = \Sigma_p(E_0 + U \times B)$, here E_0 is the background electric field, U is the neutral wind velocity, and B is the magnetic field. The westward directed plasma convection observed during the event, likely associated with SAPS, suggests that E_0 is the dominant component and is predominantly northwards. U is assumed to be much smaller compared to E_0 since the event was observed during the early phases of a storm and the role of the neutral wind (the disturbance dynamo) is expected to be significant during the recovery phase (Blanc and Richmond, 1980). Consequently, J_P is also directed northwards, in the same direction as E_0. Note that the electrodynamics during the event are significantly different from the quiet-time events (Kp = 0) reported by Suzuki et al. (2009) which assume U is the dominant component and neglect the role of E_0. To maintain current continuity, polarization electric fields are induced orthogonal to the MSTID wave fronts by J_P such that they are directed north-eastwards(south-westwards) in regions of TEC depletion(enhancement). In other words, the polarization electric field has a component in the direction of J_P in regions of reduced conductivity, and away in regions of enhanced conductivity. The scenario is illustrated in Figure 2.9. The ExB drift associated with these polarization electric fields would be directed towards (positive LOS velocities) the radar in regions with high TEC, and away (negative LOS velocities) in regions with low

TEC. Since the ExB drifts associated with the polarization electric fields are expected to be predominantly meridional, the corresponding velocity changes will be prominent in poleward-directed beams, such as beam 18 of FHW (Figure 2.8). This mechanism is consistent with the sense of the observations presented in Figures 2.7 and 2.8. For example, Figure in 2.7.b two distinct MSTID wave fronts are observed between midnight and 1:00 UT as enhancements in TEC, and corresponding SuperDARN observations show positive (blue/towards the radar) LOS velocities collocated with these enhancements.

Overall, this study presents a new class of electrified MSTIDs that are distinct from the typical quiet-time MSTIDs reported previously (Otsuka et al., 2004, 2007; Ogawa et al., 2009, e.g.,). The oscillations in SuperDARN LOS velocities and dTEC were almost an order of magnitude stronger than those observed during quiet-times (Suzuki et al., 2009) and a new mechanism has been proposed to explain the generation of polarization electric fields during intervals of strong geomagnetic driving.

2.6 Conclusions

This study has analyzed observations of MSTIDs during the September 7th/8th 2017 geomagnetic storm event, over mid-latitude North America. The event interval was characterized by strong geomagnetic driving with Kp reaching 9, and SymH dropping to nearly -200 nT. Signatures of MSTIDs were observed in both GNSS TEC and ionospheric backscatter in SuperDARN, with similar time-periods (∼15 minutes), wavelength (∼700km), and phase speeds (∼600 m/s). In SuperDARN, the MSTIDs produced oscillations ranging ±500m/s in LOS velocities, and in detrended GNSS TEC strong perturbations reaching up to 50% of the background TEC value were observed. These MSTIDs were propagating in the south-westward direction, similar to previous reports of MSTIDs observed on the nightside. Su-

perDARN data showed that the MSTID signatures were observed in both near and farther ranges, suggesting strong coupling between the E and the F-regions. Projecting detrended GNSS TEC data along SuperDARN beams showed that enhancements in TEC were positively correlated with increases in SuperDARN SNR, contrary to previous observations which showed that these parameters were anti-correlated, at least in quiet time events. Strong oscillations in LOS velocities observed in SuperDARN indicated a systematic reversal in the polarity of the electric fields between the crests and troughs of the MSTIDs, confirming the presence of polarization electric fields during the event. The poleward directed background electric fields associated with westward directed plasma convection observed during the event were hypothesized to generate the polarization electric fields. Overall, the storm-time MSTIDs reported in this study were driven by an electrodynamic instability and were distinct from previous reports of electrified MSTIDs which were observed during quiet geomagnetic intervals.

2.7 Open Research

SuperDARN data can be found at the Virginia Tech SuperDARN webpage at https://www.frdr-dfdr.ca/repo/collection/superdarn. SuperDARN data has been processed using the Radar Software Toolkit (Group et al., 2022). LOS GNSS TEC data is available at http://www.openmadrigal.org. Individual GNSS TEC data files used in this study can be found at https://w3id.org/cedar?experiment_list=experiments2/2017/gps/07sep17&file_list=los_20170907.004.h5 and https://w3id.org/cedar?experiment_list=experiments2/2017/gps/08sep17&file_list=los_20170908.004.h5. Data processing and visualization was done using open-source software, including Matplotlib (Hunter, 2007), Pandas (Wes McKinney, 2010), IPython (Pérez and Granger, 2007), Cartopy (Met

Office, 2010 - 2013), Scipy (Virtanen et al., 2020), and others (Millman and Aivazis, 2011).

2.8 Acknowledgments

The authors thank the National Science Foundation for support by grants AGS-1935110, and AGS-1952737. BSRK and JBHB acknowledge National Science Foundation for support by grants AGS-1822056, and AGS-1839509. The Christmas Valley SuperDARN radars are maintained and operated by Dartmouth College under support by NSF grant AGS-1934997. SuperDARN is a worldwide collection of radars funded by various national funding agencies of Australia, Canada, China, France, Italy, Japan, Norway, South Africa, United Kingdom, and the United States of America. SuperDARN data used in this study can be accessed from the following website: https://www.frdr-dfdr.ca/repo/collection/superdarn. The geomagnetic indices used in this paper can be obtained from NASA's OMNIWeb service (https://omniweb.gsfc.nasa.gov/form/dx1.html). GPS TEC data products and access through the Madrigal distributed data system are provided to the community by the Massachusetts Institute of Technology under support from US National Science Foundation grant AGS-1952737. Data for the TEC processing is provided from the following organizations: UNAVCO, Scripps Orbit and Permanent Array Center, Institut Geographique National, France, International GNSS Service, The Crustal Dynamics Data Information System (CDDIS), National Geodetic Survey, Instituto Brasileiro de Geografia e Estatística, RAMSAC CORS of Instituto Geográfico Nacional de la República Argentina, Arecibo Observatory, Low-Latitude Ionospheric Sensor Network (LISN), Topcon Positioning Systems, Inc., Canadian High Arctic Ionospheric Network, Institute of Geology and Geophysics, Chinese Academy of Sciences, China Meteorology Administration, Centro di Ricerche Sismologiche, Système d'Observation du Niveau des Eaux Littorales (SONEL), RENAG : REseau

NAtional GPS permanent, GeoNet - the official source of geological hazard information for New Zealand, GNSS Reference Networks, Finnish Meteorological Institute, SWEPOS - Sweden, Hartebeesthoek Radio Astronomy Observatory, TrigNet Web Application, South Africa, Australian Space Weather Services, RETE INTEGRATA NAZIONALE GPS, Estonian Land Board, Virginia Tech Center for Space Science and Engineering Research, and Korea Astronomy and Space Science Institute.

Chapter 3

Conclusions and Future Work

This research was intended to answer questions about the driving processed behind storm time MSTIDs. In Chapter 1, GNSS TEC and SuperDARN were introduced. GNSS TEC has been de-trended from a high-resolution global data product. Coverage of both datasets is sufficient for capturing MSTIDs. Their usefulness in measuring MSTIDs was shown. Additionally, geomagnetic storms were defined. TIDs, including MSTIDs were presented. The differences between AGW and electrified MSTIDs were outlined.

In Chapter 2, an event study was conducted which showed clear evidence of storm time electrified MSTIDs. This result answered an uncertainty about the same event posed in (Zhang et al., 2019) with the addition of SuperDARN data. Specifically, it was postulated that the Perkins instability (Perkins, 1973) may play a role in the MSTIDs, based on propagation direction. Using SuperDARN data confirmed that radar measurements matched nearly 1:1 with GNSS TEC observations. This was an indicator that the radars observed the MSTIDs directly, as a result of field aligned irregularities. This also suggested that AGW driving was not the primary mechanism for these MSTIDs. Furthermore, SuperDARN LOS velocity measurements were shown to oscillate in velocity (up to $\pm$500 m/s) in line with the density structures of the MSTIDs. These density structures were strong as well, reaching +40dB in peak SuperDARN power and $\sim$50 percent of background TEC. These results are indicative of polarization electric fields within the MSTID, which need to be strong enough to drive the observed plasma motion. This result shows that electrified MSTIDs are possible not only on

the night side, but during strong geomagnetic storms, including on the day side.

The relationship between storm periods and electrified MSTID behavior is a possible area of future research. Event studies of other storm intervals may be illuminating. Specifically, August 26th, 2016 was another period explored in preliminary versions, but not presented in this work. Since storm time intervals, especially Kp=9, are not common, climatological studies may be challenging. This work also only looks at North American data, and other regions may be helpful. Geomagnetic conjugacy is further proof of electrified MSTID driving. A Study using GNSS TEC and SuperDARN in both hemispheres (similar to (Otsuka et al., 2004)) would help solidify the results of this work. TEC coverage in the Southern Hemisphere is poor. However, even a few active receivers may be sufficient to show MSTID signatures. Other datasets may be beneficial for resolving remaining questions. Mainly the issue of E vs F region driving needs to be resolved fully. Incoherent scatter radars within the MSTID structure would help resolve this issue, through altitude dependent measurements of electron density. Also, enhancing the use of SuperDARN and TEC could resolve this question. Altitude information in SuperDARN can be obtained with accurate elevation angle measurements. GNSS TEC can be used to find electron density as a function of altitude when multiple IPP paths intersect. This process is known as TEC tomography. Finally, GNSS TEC processing outlined in Chapter 1 may not be optimal, and a more comprehensive process such as the one used in (Zhang et al., 2019) may enhance MSTID signatures. However, this may not be as consequential in this study since MSTID signatures reached $\sim$50 percent of background TEC. Through the use of more types of data and better use of existing data, the processes behind storm time electrified MSTIDs may be better understood in the future.

Bibliography

D. André, G. J. Sofko, K. Baker, and J. MacDougall. Superdarn interferometry: Meteor echoes and electron densities from groundscatter. *Journal of Geophysical Research: Space Physics*, 103:7003–7015, 4 1998. ISSN 21699402. doi: 10.1029/97ja02923.

A. Angrisano, M. Petovello, and G. Pugliano. Benefits of combined gps/glonass with low-cost mems imus for vehicular urban navigation. *Sensors*, 12:5134–5158, 4 2012. ISSN 14248220. doi: 10.3390/s120405134.

J. B.H. Baker, R. A. Greenwald, J. M. Ruohoniemi, K. Oksavik, J. W. Gjerloev, L. J. Paxton, and M. R. Hairston. Observations of ionospheric convection from the wallops superdarn radar at middle latitudes. *Journal of Geophysical Research: Space Physics*, 112:1303, 1 2007. ISSN 2156-2202. doi: 10.1029/2006JA011982.

K. B. Baker, R. A. Greenwald, J. M. Ruohoniemi, J. R. Dudeney, M. Pinnock, N. Mattin, and J. M. Leonard. Polar anglo-american conjugate experiment. *Eos, Transactions American Geophysical Union*, 70:785–799, 1989. ISSN 23249250. doi: 10.1029/89EO00253.

R. Behnke. F layer height bands in the nocturnal ionosphere over arecibo. *Journal of Geophysical Research: Space Physics*, 84:974–978, 3 1979. ISSN 2156-2202. doi: 10.1029/JA084IA03P00974.

M. Blanc and A.D. Richmond. The ionospheric disturbance dynamo. *Journal of Geophysical Research: Space Physics*, 85(A4):1669–1686, 1980. doi: https://doi.org/10.1029/JA085iA04p01669.

C. Borries, N. Jakowski, and V. Wilken. Storm induced large scale tids observed in gps

derived tec. *Annales Geophysicae*, 27:1605–1612, 2009. ISSN 09927689. doi: 10.5194/ANGEO-27-1605-2009.

W. A. Bristow, R. A. Greenwald, and J. C. Samson. Identification of high-latitude acoustic gravity wave sources using the goose bay hf radar. *Journal of Geophysical Research: Space Physics*, 99:319–331, 1 1994. ISSN 2156-2202. doi: 10.1029/93JA01470.

W. A. Bristow, R. A. Greenwald, and J. P. Villain. On the seasonal dependence of medium-scale atmospheric gravity waves in the upper atmosphere at high latitudes. *Journal of Geophysical Research: Space Physics*, 101:15685–15699, 7 1996. ISSN 2156-2202. doi: 10.1029/96JA01010.

G. Chimonas and C. O. Hines. Atmospheric gravity waves launched by auroral currents. *Planetary and Space Science*, 18:565–582, 4 1970. ISSN 0032-0633. doi: 10.1016/0032-0633(70)90132-7.

G Chisham, Ae M Lester, Ae S E Milan, Ae M P Freeman, Ae W A Bristow, Ae A Grocott, Ae K A Mcwilliams, Ae J M Ruohoniemi, Ae T K Yeoman, Ae P L Dyson, Ae R A Greenwald, Ae T Kikuchi, Ae M Pinnock, Ae J P S Rash, Ae N Sato, Ae G J Sofko, J.-P Villain, Ae A D M Walker, M P Freeman, Á M Pinnock, M Lester, Á S E Milan, Á A Grocott, T K Yeoman, W A Bristow, K A Mcwilliams, Á G J Sofko, J M Ruohoniemi, R A Greenwald, P L Dyson, T Kikuchi, J P S Rash, Á A D M Walker, and N Sato. A decade of the super dual auroral radar network (superdarn): scientific achievements, new techniques and future directions. *Surveys in Geophysics 2007 28:1*, 28:33–109, 5 2007. ISSN 1573-0956. doi: 10.1007/S10712-007-9017-8.

G. Chisham, T. K. Yeoman, and G. J. Sofko. Mapping ionospheric backscatter measured by the superdarn hf radars – part 1: A new empirical virtual height model. *Annales Geophysicae*, 26(4):823–841, 2008. doi: 10.5194/angeo-26-823-2008.

Min Yang Chou, Charles C.H. Lin, Jia Yue, Ho Fang Tsai, Yang Yi Sun, Jann Yenq Liu, and Chia Hung Chen. Concentric traveling ionosphere disturbances triggered by super typhoon meranti (2016). *Geophysical Research Letters*, 44:1219–1226, 2 2017. ISSN 1944-8007. doi: 10.1002/2016GL072205.

A. Coster, J. Williams, A. Weatherwax, W. Rideout, and D. Herne. Accuracy of gps total electron content: Gps receiver bias temperature dependence. *Radio Science*, 48:190–196, 3 2013. ISSN 1944-799X. doi: 10.1002/RDS.20011.

A. J. Coster, L. Goncharenko, S. R. Zhang, P. J. Erickson, W. Rideout, and J. Vierinen. Gnss observations of ionospheric variations during the 21 august 2017 solar eclipse. *Geophysical Research Letters*, 44:12,041–12,048, 12 2017. ISSN 1944-8007. doi: 10.1002/2017GL075774.

T. Neil Davis and Masahisa Sugiura. Auroral electrojet activity index ae and its universal time variations. *Journal of Geophysical Research (1896-1977)*, 71(3):785–801, 1966. doi: https://doi.org/10.1029/JZ071i003p00785.

F. Ding, W. Wan, B. Ning, and M. Wang. Large-scale traveling ionospheric disturbances observed by gps total electron content during the magnetic storm of 29–30 october 2003. *Journal of Geophysical Research: Space Physics*, 112:6309, 6 2007. ISSN 2156-2202. doi: 10.1029/2006JA012013.

T. M. Duly, N. P. Chapagain, and J. J. Makela. Climatology of nighttime medium-scale traveling ionospheric disturbances (mstids) in the central pacific and south american sectors. *Annales Geophysicae*, 31:2229–2237, 12 2013. ISSN 09927689. doi: 10.5194/ANGEO-31-2229-2013.

M. P. Freeman, J. M. Ruohoniemi, and R. A. Greenwald. The determination of time-

stationary two-dimensional convection patterns with single-station radars. *Journal of Geophysical Research: Space Physics*, 96:15735–15749, 9 1991. doi: 10.1029/91ja00445.

N. A. Frissell, J. B.H. Baker, J. M. Ruohoniemi, A. J. Gerrard, E. S. Miller, J. P. Marini, M. L. West, and W. A. Bristow. Climatology of medium-scale traveling ionospheric disturbances observed by the midlatitude blackstone superdarn radar. *Journal of Geophysical Research: Space Physics*, 119:7679–7697, 2014. ISSN 21699402. doi: 10.1002/2014JA019870.

N. A. Frissell, J. B. H. Baker, J. M. Ruohoniemi, R. A. Greenwald, A. J. Gerrard, E. S. Miller, and M. L. West. Sources and characteristics of medium-scale traveling ionospheric disturbances observed by high-frequency radars in the north american sector. *Journal of Geophysical Research: Space Physics*, 121:3722–3739, 4 2016. ISSN 2169-9380. doi: 10.1002/2015JA022168.

Shoichiro Fukao, Michael C. Kelley, Tatsuya Shirakawa, Tomoyuki Takami, Mamoru Yamamoto, Toshitaka Tsuda, and Susumu Kato. Turbulent upwelling of the mid-latitude ionosphere: 1. observational results by the mu radar. *Journal of Geophysical Research: Space Physics*, 96:3725–3746, 3 1991. ISSN 2156-2202. doi: 10.1029/90JA02253.

F. J. Garcia, M. C. Kelley, J. J. Makela, and C. S. Huang. Airglow observations of mesoscale low-velocity traveling ionospheric disturbances at midlatitudes. *Journal of Geophysical Research: Space Physics*, 105:18407–18415, 8 2000. ISSN 2156-2202. doi: 10.1029/1999JA000305.

T. M. Georges. Hf doppler studies of traveling ionospheric disturbances. *Journal of Atmospheric and Terrestrial Physics*, 30:735–746, 1 1968. ISSN 0021-9169. doi: 10.1016/S0021-9169(68)80029-7.

I. A. Getting. The global positioning system. *IEEE Spectrum*, 30:36–38, 1993. ISSN 00189235. doi: 10.1109/6.272176.

R. A. Greenwald. History of the super dual auroral radar network (superdarn)-i: pre-superdarn developments in high frequency radar technology for ionospheric research and selected scientific results. *History of Geo- and Space Sciences*, 12:77–93, 5 2021. ISSN 21905029. doi: 10.5194/hgss-12-77-2021.

R. A. Greenwald, W. Weiss, E. Nielsen, and N. R. Thomson. Stare: A new radar auroral backscatter experiment in northern scandinavia. *Radio Science*, 13:1021–1039, 11 1978. ISSN 00486604. doi: 10.1029/RS013i006p01021.

R. A. Greenwald, K. B. Baker, R. A. Hutchins, and C. Hanuise. An hf phased-array radar for studying small-scale structure in the high-latitude ionosphere. *Radio Science*, 20:63–79, 1 1985. ISSN 00486604. doi: 10.1029/RS020i001p00063.

R. A. Greenwald, K. B. Baker, J. R. Dudeney, M. Pinnock, T. B. Jones, E. C. Thomas, J. P. Villain, J. C. Cerisier, C. Senior, C. Hanuise, R. D. Hunsucker, G. Sofko, J. Koehler, E. Nielsen, R. Pellinen, A. D.M. Walker, N. Sato, and H. Yamagishi. Darn/superdarn. *Space Science Reviews 1995 71:1*, 71:761–796, 2 1995. ISSN 1572-9672. doi: 10.1007/BF00751350.

A. Grocott, K. Hosokawa, T. Ishida, M. Lester, S. E. Milan, M. P. Freeman, N. Sato, and A. S. Yukimatu. Characteristics of medium-scale traveling ionospheric disturbances observed near the antarctic peninsula by hf radar. *Journal of Geophysical Research: Space Physics*, 118:5830–5841, 9 2013. ISSN 2169-9402. doi: 10.1002/JGRA.50515.

SuperDARN Data Analysis Working Group, A.G. Burrell, E.G. Thomas, M.T. Schmidt, E.C. Bland, I. Coco, P.V. Ponomarenko, K.T. Sterne, and M.-T. Walach. Superdarn/rst: Rst 4.7, April 2022. URL https://doi.org/10.5281/zenodo.6473603.

W. H. Guier and G. C. Weiffenbach. A satellite doppler navigation system. *Proceedings of the IRE*, 48:507–516, 1960. ISSN 00968390. doi: 10.1109/JRPROC.1960.287399.

Jia-Peng Guo, Yue Deng, Dong-He Zhang, Yang Lu, Cheng Sheng, and Shun-Rong Zhang. The effect of subauroral polarization streams on ionosphere and thermosphere during the 2015 st. patrick's day storm: Global ionosphere-thermosphere model simulations. *Journal of Geophysical Research: Space Physics*, 123:2241–2256, 3 2018. ISSN 2169-9380. doi: 10.1002/2017JA024781.

K. Hansen and J. Stevens. Clouds near australia. *NASA Earth Observatory*, 10 2017. URL https://earthobservatory.nasa.gov/images/91192/clouds-near-australia?src=ve.

W. Hazeyama, N. Nishitani, T. Hori, T. Nakamura, and S. Perwitasari. Statistical study of seasonal and solar activity dependence of nighttime mstids occurrence using the superdarn hokkaido pair of radars. *Journal of Geophysical Research: Space Physics*, 127: e2021JA029965, 4 2022. ISSN 2169-9402. doi: 10.1029/2021JA029965.

C. O. Hines. Internal atmospheric gravity waves at ionospheric heights. *Canadian Journal of Physics*, 38:1441–1481, 11 1960. ISSN 0008-4204. doi: 10.1139/P60-150.

Alicreance Hiyadutuje, Michael J. Kosch, and Judy A. E. Stephenson. First observations of e-region near range echoes partially modulated by f-region traveling ionospheric disturbances observed by the same superdarn hf radar. *Journal of Geophysical Research: Space Physics*, 127:e2021JA030157, 5 2022. ISSN 2169-9402. doi: 10.1029/2021JA030157.

K. Hocke and K. Schlegel. A review of atmospheric gravity waves and travelling ionospheric disturbances: 1982-1995. *Annales Geophysicae*, 14:917–940, 9 1996. doi: 10.1007/S00585-996-0917-6.

Klemens Hocke, Huixin Liu, Nicholas Pedatella, and Guanyi Ma. Global sounding of f region irregularities by cosmic during a geomagnetic storm. *Annales Geophysicae*, 37:235–242, 4 2019. ISSN 14320576. doi: 10.5194/ANGEO-37-235-2019.

Fuqing Huang, Xiankang Dou, Jiuhou Lei, Jian Lin, Feng Ding, and Jiahao Zhong. Statistical analysis of nighttime medium-scale traveling ionospheric disturbances using airglow images and gps observations over central china. *Journal of Geophysical Research: Space Physics*, 121:8887–8899, 9 2016. ISSN 2169-9402. doi: 10.1002/2016JA022760.

Robert D. Hunsucker. Atmospheric gravity waves generated in the high-latitude ionosphere: A review. *Reviews of Geophysics*, 20:293–315, 5 1982. ISSN 1944-9208. doi: 10.1029/RG020I002P00293.

J. D. Hunter. Matplotlib: A 2d graphics environment. *Computing In Science & Engineering*, 9(3):90–95, 2007. doi: 10.1109/MCSE.2007.55.

Toshihiko Iyemori. Storm-time magnetospheric currents inferred from mid-latitude geomagnetic field variations. *Journal of geomagnetism and geoelectricity*, 42:1249–1265, 1990. ISSN 0022-1392. doi: 10.5636/jgg.42.1249.

Olusegun F. Jonah, Panagiotis Vergados, Siddharth Krishnamoorthy, and Attila Komjathy. Investigating ionospheric perturbations following the 2020 beirut explosion event. *Radio Science*, 56:e2021RS007302, 10 2021. ISSN 1944-799X. doi: 10.1029/2021RS007302.

I. J. Kelley, B. S. R. Kunduri, J. B. H. Baker, J. M. Ruohoniemi, and S. G. Shepherd. Storm time electrified mstids observed over mid-latitude north america. *Earth and Space Science Open Archive*, page 21, 2022. doi: 10.1002/essoar.10511903.1.

M. C. Kelley. *The earth's ionosphere : plasma physics and electrodynamics*. Academic Press, 2009. ISBN 9780080916576.

M. C. Kelley. On the origin of mesoscale tids at midlatitudes. *Annales Geophysicae*, 29: 361–366, 2011. ISSN 09927689. doi: 10.5194/ANGEO-29-361-2011.

M. C. Kelley and S. Fukao. Turbulent upwelling of the mid-latitude ionosphere: 2. theoretical framework. *Journal of Geophysical Research: Space Physics*, 96:3747–3753, 3 1991. ISSN 2156-2202. doi: 10.1029/90JA02252.

J. H. King and N. E. Papitashvili. Solar wind spatial scales in and comparisons of hourly wind and ace plasma and magnetic field data. *Journal of Geophysical Research*, 110: A02104, 2 2005. ISSN 0148-0227. doi: 10.1029/2004JA010649.

J. A. Klobuchar. Ionospheric time-delay algorithm for single-frequency gps users. *IEEE Transactions on Aerospace and Electronic Systems*, AES-23:325–331, 1987. ISSN 00189251. doi: 10.1109/TAES.1987.310829.

N. Kotake, Y. Otsuka, T. Tsugawa, T. Ogawa, and A. Saito. Climatological study of gps total electron content variations caused by medium-scale traveling ionospheric disturbances. *Journal of Geophysical Research: Space Physics*, 111, 4 2006. ISSN 21699402. doi: 10.1029/2005JA011418.

B. S. R. Kunduri, J. B. H. Baker, J. M. Ruohoniemi, N. Nishitani, K. Oksavik, P. J. Erickson, A. J. Coster, S. G. Shepherd, W. A. Bristow, and E. S. Miller. A new empirical model of the subauroral polarization stream. *Journal of Geophysical Research: Space Physics*, 123 (9):7342–7357, 2018. doi: https://doi.org/10.1029/2018JA025690.

V. E. Kunitsyn, A. M. Padokhin, G. A. Kurbatov, Yu V. Yasyukevich, and Yu V. Morozov. Ionospheric tec estimation with the signals of various geostationary navigational satellites. *GPS Solutions*, 20:877–884, 10 2016. ISSN 15211886. doi: 10.1007/s10291-015-0500-2.

R. S. Lawrence, D. J. Posakony, O. K. Garriott, and S. C. Hall. The total electron content of the ionosphere at middle latitudes near the peak of the solar cycle. *Journal of Geophysical Research*, 68:1889–1898, 4 1963. ISSN 2156-2202. doi: 10.1029/JZ068I007P01889.

Jann-Yenq Liu, Chia-Hung Chen, Chien-Hung Lin, Ho-Fang Tsai, Chieh-Hung Chen, Masashi Kamogawa, Citation : Liu, C.-H Chen, C.-H Lin, H.-F Tsai, and M Kamogawa. Ionospheric disturbances triggered by the 11 march 2011 m9.0 tohoku earthquake. *Journal of Geophysical Research: Space Physics*, 116:6319, 6 2011. ISSN 2156-2202. doi: 10.1029/2011JA016761.

L. R. Lyons, Y. Nishimura, S. R. Zhang, A. J. Coster, A. Bhatt, E. Kendall, and Y. Deng. Identification of auroral zone activity driving large-scale traveling ionospheric disturbances. *Journal of Geophysical Research: Space Physics*, 124:700–714, 1 2019. ISSN 2169-9402. doi: 10.1029/2018JA025980.

A. G. McNamara, D. R. McDiarmid, G. J. Sofko, J. A. Koehler, P. A. Forsyth, and D. R. Moorcroft. Bars - a dual bistatic auroral radar system for the study of electric fields in the canadian sector of the auroral zone. *Advances in Space Research*, 2:145–148, 1 1982. ISSN 02731177. doi: 10.1016/0273-1177(82)90164-8.

Michael Mendillo, Jeffrey Baumgardner, Daniel Nottingham, Jules Aarons, Bodo Reinisch, James Scali, and Michael Kelley. Investigations of thermospheric-ionospheric dynamics with 6300-Å images from the arecibo observatory. *Journal of Geophysical Research: Space Physics*, 102:7331–7343, 4 1997. doi: 10.1029/96JA02786.

Met Office. *Cartopy: a cartographic python library with matplotlib support*. Exeter, Devon, 2010 - 2013. URL https://scitools.org.uk/cartopy.

C. M. Michael, T. K. Yeoman, D. M. Wright, S. E. Milan, and M. K. James. A ray tracing simulation of hf ionospheric radar performance at african equatorial latitudes. *Radio Science*, 55:e2019RS006936, 2 2020. ISSN 0048-6604. doi: 10.1029/2019RS006936.

Clark A. Miller. Electrodynamics of midlatitude spread f 2. a new theory of gravity wave

electric fields. *Journal of Geophysical Research: Space Physics*, 102:11533–11538, 6 1997. ISSN 2156-2202. doi: 10.1029/96JA03840.

K. Jarrod Millman and Michael Aivazis. Python for scientists and engineers. *Computing in Science & Engineering*, 13(2):9–12, March-April 2011. doi: 10.1109/MCSE.2011.36.

C. N. Mitchell, L. Alfonsi, G. De Franceschi, M. Lester, V. Romano, and A. W. Wernik. Gps tec and scintillation measurements from the polar ionosphere during the october 2003 storm. *Geophysical Research Letters*, 32:1–4, 6 2005. ISSN 1944-8007. doi: 10.1029/2004GL021644.

G. H. Munro. Short-period changes in the f region of the ionosphere. *Nature 1948 162:4127*, 162:886–887, 1948. ISSN 1476-4687. doi: 10.1038/162886a0.

V. L. Narayanan, K. Shiokawa, Y. Otsuka, and D. Neudegg. On the role of thermospheric winds and sporadic e layers in the formation and evolution of electrified mstids in geomagnetic conjugate regions. *Journal of Geophysical Research: Space Physics*, 123:6957–6980, 8 2018. ISSN 2169-9402. doi: 10.1029/2018JA025261.

E. Nielsen, W. Güttler, E. C. Thomas, C. P. Stewart, T. B. Jones, and A. Hedberg. A new radar auroral backscatter experiment. *Nature*, 304:712–714, 8 1983. ISSN 00280836. doi: 10.1038/304712a0.

Nozomu Nishitani, John Michael Ruohoniemi, Mark Lester, Joseph Benjamin Harold Baker, Alexandre Vasilyevich Koustov, Simon G. Shepherd, Gareth Chisham, Tomoaki Hori, Evan G. Thomas, Roman A. Makarevich, Aurélie Marchaudon, Pavlo Ponomarenko, James A. Wild, Stephen E. Milan, William A. Bristow, John Devlin, Ethan Miller, Raymond A. Greenwald, Tadahiko Ogawa, and Takashi Kikuchi. Review of the accomplishments of mid-latitude super dual auroral radar network (superdarn) hf radars.

Progress in Earth and Planetary Science 2019 6:1, 6:1–57, 3 2019. ISSN 2197-4284. doi: 10.1186/S40645-019-0270-5.

T. Ogawa, N. Nishitani, Y. Otsuka, K. Shiokawa, T. Tsugawa, and K. Hosokawa. Medium-scale traveling ionospheric disturbances observed with the superdarn hokkaido radar, all-sky imager, and gps network and their relation to concurrent sporadic e irregularities. *Journal of Geophysical Research: Space Physics*, 114:3316, 3 2009. ISSN 2156-2202. doi: 10.1029/2008JA013893.

Y. Otsuka, K. Shiokawa, T. Ogawa, and P. Wilkinson. Geomagnetic conjugate observations of medium-scale traveling ionospheric disturbances at midlatitude using all-sky airglow imagers. *Geophysical Research Letters*, 31, 8 2004. ISSN 1944-8007. doi: 10.1029/2004GL020262.

Y. Otsuka, F. Onoma, K. Shiokawa, T. Ogawa, M. Yamamoto, and S. Fukao. Simultaneous observations of nighttime medium-scale traveling ionospheric disturbances and e region field-aligned irregularities at midlatitude. *Journal of Geophysical Research: Space Physics*, 112:6317, 6 2007. ISSN 2156-2202. doi: 10.1029/2005JA011548.

Y. Otsuka, K. Shiokawa, T. Ogawa, T. Yokoyama, and M. Yamamoto. Spatial relationship of nighttime medium-scale traveling ionospheric disturbances and f region field-aligned irregularities observed with two spaced all-sky airglow imagers and the middle and upper atmosphere radar. *Journal of Geophysical Research: Space Physics*, 114, 5 2009. ISSN 21699402. doi: 10.1029/2008JA013902.

Y. Otsuka, K. Suzuki, S. Nakagawa, M. Nishioka, K. Shiokawa, and T. Tsugawa. Gps observations of medium-scale traveling ionospheric disturbances over europe. *Annales Geophysicae*, 31:163–172, 2013. ISSN 09927689. doi: 10.5194/angeo-31-163-2013.

Fernando Pérez and Brian E. Granger. IPython: a system for interactive scientific computing. *Computing in Science and Engineering*, 9(3):21–29, May 2007. ISSN 1521-9615. doi: 10.1109/MCSE.2007.53. URL http://ipython.org.

Francis Perkins. Spread f and ionospheric currents. *Journal of Geophysical Research*, 78: 218–226, 1 1973. ISSN 0148-0227. doi: 10.1029/JA078I001P00218.

William Rideout and Anthea Coster. Automated gps processing for global total electron content data. *GPS Solutions*, 10:219–228, 7 2006. ISSN 10805370.

J. M. Ruohoniemi and K. B. Baker. Large-scale imaging of high-latitude convection with super dual auroral radar network hf radar observations. *Journal of Geophysical Research: Space Physics*, 103:20797–20811, 9 1998. ISSN 21699402. doi: 10.1029/98JA01288.

J. M. Ruohoniemi, R. A. Greenwald, K. B. Baker, J. P. Villain, and M. A. McCready. Drift motions of small-scale irregularities in the high-latitude f region: An experimental comparison with plasma drift motions. *Journal of Geophysical Research: Space Physics*, 92:4553–4564, 5 1987. ISSN 2156-2202. doi: 10.1029/JA092IA05P04553.

J. M. Ruohoniemi, R. A. Greenwald, K. B. Baker, J.-P. Villain, C. Hanuise, and J. Kelly. Mapping high-latitude plasma convection with coherent hf radars. *Journal of Geophysical Research*, 94:13463, 10 1989. ISSN 0148-0227. doi: 10.1029/ja094ia10p13463.

A. Saito, T. Iyemori, M. Sugiura, N. C. Maynard, T. L. Aggson, L. H. Brace, M. Takeda, and M. Yamamoto. Conjugate occurrence of the electric field fluctuations in the nighttime midlatitude ionosphere. *Journal of Geophysical Research: Space Physics*, 100:21439–21451, 11 1995. ISSN 2156-2202. doi: 10.1029/95JA01505.

A. Saito, S. Fukao, and S. Miyazaki. High resolution mapping of tec perturbations with the

gsi gps network over japan. *Geophysical Research Letters*, 25:3079–3082, 8 1998. ISSN 1944-8007. doi: 10.1029/98GL52361.

J. C. Samson, R. A. Greenwald, J. M. Ruohoniemi, A. Frey, and K. B. Baker. Goose bay radar observations of earth-reflected, atmospheric gravity waves in the high-latitude ionosphere. *Journal of Geophysical Research: Space Physics*, 95:7693–7709, 6 1990. ISSN 2156-2202. doi: 10.1029/JA095IA06P07693.

K. Shiokawa, Y. Otsuka, C. Ihara, T. Ogawa, and F. J. Rich. Ground and satellite observations of nighttime medium-scale traveling ionospheric disturbance at midlatitude. *Journal of Geophysical Research: Space Physics*, 108, 4 2003. ISSN 2156-2202. doi: 10.1029/2002JA009639.

K. T. Sterne, R. A. Greenwald, J. B.H. Baker, and J. M. Ruohoniemi. Modeling of a twin terminated folded dipole antenna for the super dual auroral radar network (superdarn). *IEEE National Radar Conference - Proceedings*, pages 934–938, 2011. ISSN 10975659. doi: 10.1109/RADAR.2011.5960673.

S. Suzuki, K. Hosokawa, Y. Otsuka, K. Shiokawa, T. Ogawa, N. Nishitani, T. F. Shibata, A. V. Koustov, and B. M. Shevtsov. Coordinated observations of nighttime medium-scale traveling ionospheric disturbances in 630-nm airglow and hf radar echoes at midlatitudes. *Journal of Geophysical Research: Space Physics*, 114:7312, 7 2009. ISSN 2156-2202. doi: 10.1029/2008JA013963.

T. Tsugawa, Y. Otsuka, A. J. Coster, and A. Saito. Medium-scale traveling ionospheric disturbances detected with dense and wide tec maps over north america. *Geophysical Research Letters*, 34:22101, 11 2007. ISSN 1944-8007. doi: 10.1029/2007GL031663.

R. T. Tsunoda and R. B. Cosgrove. Coupled electrodynamics in the nighttime midlatitude

ionosphere. *Geophysical Research Letters*, 28:4171–4174, 11 2001. ISSN 1944-8007. doi: 10.1029/2001GL013245.

Sharon L. Vadas. Horizontal and vertical propagation and dissipation of gravity waves in the thermosphere from lower atmospheric and thermospheric sources. *Journal of Geophysical Research: Space Physics*, 112:n/a–n/a, 6 2007. ISSN 01480227. doi: 10.1029/2006JA011845.

C. E. Valladares and R. Sheehan. Observations of conjugate mstids using networks of gps receivers in the american sector. *Radio Science*, 51:1470–1488, 9 2016. ISSN 1944-799X. doi: 10.1002/2016RS005967.

Juha Vierinen, Anthea J. Coster, William C. Rideout, Philip J. Erickson, and Johannes Norberg. Statistical framework for estimating gnss bias. *Atmospheric Measurement Techniques*, 9:1303–1312, 3 2016. ISSN 18678548. doi: 10.5194/AMT-9-1303-2016.

Pauli Virtanen, Ralf Gommers, Travis E. Oliphant, Matt Haberland, Tyler Reddy, David Cournapeau, Evgeni Burovski, Pearu Peterson, Warren Weckesser, Jonathan Bright, Stéfan J. van der Walt, Matthew Brett, Joshua Wilson, K. Jarrod Millman, Nikolay Mayorov, Andrew R. J. Nelson, Eric Jones, Robert Kern, Eric Larson, C J Carey, İlhan Polat, Yu Feng, Eric W. Moore, Jake VanderPlas, Denis Laxalde, Josef Perktold, Robert Cimrman, Ian Henriksen, E. A. Quintero, Charles R. Harris, Anne M. Archibald, Antônio H. Ribeiro, Fabian Pedregosa, Paul van Mulbregt, and SciPy 1.0 Contributors. SciPy 1.0: Fundamental Algorithms for Scientific Computing in Python. *Nature Methods*, 17:261–272, 2020. doi: 10.1038/s41592-019-0686-2.

Wes McKinney. Data Structures for Statistical Computing in Python. In Stéfan van der Walt and Jarrod Millman, editors, *Proceedings of the 9th Python in Science Conference*, pages 56 – 61, 2010. doi: 10.25080/Majora-92bf1922-00a.

Shun Rong Zhang, Philip J. Erickson, Larisa P. Goncharenko, Anthea J. Coster, William Rideout, and Juha Vierinen. Ionospheric bow waves and perturbations induced by the 21 august 2017 solar eclipse. *Geophysical Research Letters*, 44:12,067–12,073, 12 2017a. ISSN 1944-8007. doi: 10.1002/2017GL076054.

Shun Rong Zhang, Philip J. Erickson, Anthea J. Coster, William Rideout, Juha Vierinen, Olusegun Jonah, and Larisa P. Goncharenko. Subauroral and polar traveling ionospheric disturbances during the 7–9 september 2017 storms. *Space Weather*, 17:1748–1764, 12 2019. ISSN 15427390. doi: 10.1029/2019SW002325.

Shun-Rong Zhang, Philip J. Erickson, Yongliang Zhang, Wenbin Wang, Chaosong Huang, Anthea J. Coster, John M. Holt, John F. Foster, Michael Sulzer, and Robert Kerr. Observations of ion-neutral coupling associated with strong electrodynamic disturbances during the 2015 st. patrick's day storm. *Journal of Geophysical Research: Space Physics*, 122: 1314–1337, 1 2017b. ISSN 2169-9380. doi: 10.1002/2016JA023307.

Qina Zhou and John D. Mathews. On the physical explanation of the perkins instability. *Journal of Geophysical Research: Space Physics*, 111:12309, 12 2006. ISSN 2156-2202. doi: 10.1029/2006JA011696.